

WL-TR-94-3131



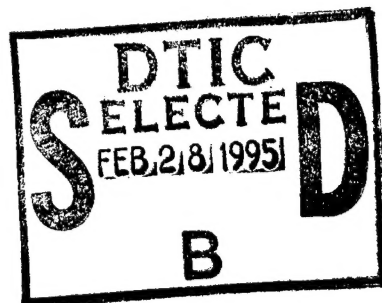
SURVEY OF CFD APPLICATIONS FOR HIGH SPEED INLETS

Keith E. Numbers

**Aerodynamics and Aero Components Research Branch
Aeromechanics Division**

July 1994

Final Report for Period August 1992 - July 1994



Approved for Public Release; Distribution Unlimited

**FLIGHT DYNAMICS DIRECTORATE
WRIGHT LABORATORY
AIR FORCE MATERIEL COMMAND
WRIGHT-PATTERSON AFB OH 45433-7913**

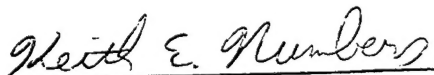
19950217 043

NOTICE

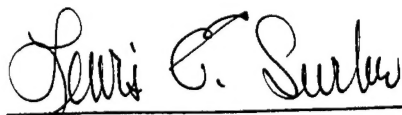
When Government drawings, specifications, or other data are used for any purpose other than in connection with a definitely Government-related procurement, the United States Government incurs no responsibility or any obligation whatsoever. The fact that the government may have formulated or in any way supplied the said drawings, specifications, or other data, is not to be regarded by implication, or otherwise in any manner construed, as licensing the holder, or any other person or corporation; or as conveying any rights or permission to manufacture, use, or sell any patented invention that may in any way be related thereto.

This report is releasable to the National Technical Information Service (NTIS). At NTIS, it will be available to the general public, including foreign nations.

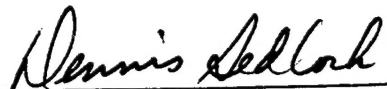
This technical report has been reviewed and is approved for publication.



Keith E. Numbers
Aerospace Engineer
Airframe Propulsion & Weapons
Integration Section



LEWIS E. SURBER
Acting Chief, Aerodynamics
and Aerocomponents
Research Branch



DENNIS SEDLOCK
Chief
Aeromechanics Division

If your address has changed, if you wish to be removed from our mailing list, or if the addressee is no longer employed by your organization please notify WL/FIMA, WPAFB, OH 45433-7913 to help us maintain a current mailing list.

Copies of this report should not be returned unless return is required by security considerations, contractual obligations, or notice on a specific document.

REPORT DOCUMENTATION PAGE			Form Approved OMB No. 0704-0188	
<small>Public reporting burden for this collection of information is estimated to average 1 hour per response, including the time for reviewing instructions, searching existing data sources, gathering and maintaining the data needed, and completing and reviewing the collection of information. Send comments regarding this burden estimate or any aspect of this collection of information, including suggestions for reducing this burden, to Washington Headquarters Services, Directorate for Information Operations and Reports, 1215 Jefferson Davis Highway, Suite 1204, Arlington, VA 22202-4302, and to the Office of Management and Budget, Paperwork Reduction Project (0704-0188), Washington, DC 20503.</small>				
1. AGENCY USE ONLY (leave blank)		2. REPORT DATE July 1994	3. REPORT TYPE AND DATES COVERED Final August 1992 - July 1994	
4. TITLE AND SUBTITLE Survey of CFD Applications for High Speed Inlets			5. FUNDING NUMBERS PE 62201F PR 2404 TA 10 WU B5	
6. AUTHOR(S) Keith E. Numbers				
7. PERFORMING ORGANIZATION NAME(S) AND ADDRESS(ES) Flight Dynamics Directorate Wright Laboratory Air Force Materiel Command Wright Patterson AFB, OH 45433-7562			8. PERFORMING ORGANIZATION REPORT NUMBER	
9. SPONSORING / MONITORING AGENCY NAME(S) AND ADDRESS(ES) Flight Dynamics Directorate Wright Laboratory Air Force Materiel Command Wright Patterson AFB, OH 45433-7562			10. SPONSORING / MONITORING AGENCY REPORT NUMBER WL-TR-94-3131	
11. SUPPLEMENTARY NOTES				
12a. DISTRIBUTION / AVAILABILITY STATEMENT Approved for Public Release; Distribution is Unlimited.			12b. DISTRIBUTION CODE	
13. ABSTRACT (Maximum 200 words) A comprehensive review of techniques and methods for applying computational fluid dynamics (CFD) analysis to high speed inlets and related flows is provided via an extensive literature survey of such applications. Topics covered include governing equations, numerical integration schemes, boundary conditions, gridding requirements, and turbulence models. Results of applications from the literature survey shed light on the relative success of the techniques being used throughout the industry.				
DTIC QUALITY INSPECTED 4				
14. SUBJECT TERMS Inlets, High Speed; Computational Fluid Dynamics; Shock wave-Boundary layer interactions.			15. NUMBER OF PAGES 62	
			16. PRICE CODE	
17. SECURITY CLASSIFICATION OF REPORT UNCLASSIFIED	18. SECURITY CLASSIFICATION OF THIS PAGE UNCLASSIFIED	19. SECURITY CLASSIFICATION OF ABSTRACT UNCLASSIFIED	20. LIMITATION OF ABSTRACT UNLIMITED	

CONTENTS

LIST OF FIGURES	iv
1.0 INTRODUCTION	1
2.0 GOVERNING EQUATIONS	3
2.1 Gas Properties	4
2.2 Time Averaged Turbulent Stress and Heat Transfer	8
2.3 Subsets of the Navier-Stokes Equations	12
2.3.1 Thin Layer Navier-Stokes	12
2.3.2 Parabolized Navier-Stokes	13
2.3.3 Euler Equations	22
3.0 NUMERICAL INTEGRATION SCHEME	25
4.0 BOUNDARY CONDITIONS	26
4.1 Freestream/Inflow Conditions	26
4.2 Wall Boundaries	27
4.3 Bleed Boundary Conditions	29
4.4 Supersonic Outflow Boundaries	32
4.5 Subsonic Outflow Boundaries	33
5.0 GRID REQUIREMENTS	36
5.1 Shock Wave Resolution	36
5.2 Boundary Layer Resolution	36
6.0 TURBULENCE MODELS AND TRANSITIONS SIMULATIONS	40
6.1 Zero-Equation Models	40
6.2 Two-Equation Models	47
6.3 Boundary Layer Transition Models	50
7.0 COMMENTS	52
REFERENCES	53

Accession For	
NTIS GRA&I	<input checked="" type="checkbox"/>
DTIC TAB	<input type="checkbox"/>
Unannounced	<input type="checkbox"/>
Justification	
By	
Distribution	
Availability Codes	
Dist	Avail and/or Special
A-1	

LIST OF FIGURES

1-1	Survey Applications	2
2-1	Coordinate Transformation Schematic	7
2-2	NASA P8 Inlet (Ref. 10)	7
2-3	P8 Calculations with High Temperature Gas Models (Ref. 9)	9
2-4	Unsteady Mean Flow with Fluctuating Components	11
2-5a	Mixed Compression Inlet Application (Ref. 12)	11
2-5b	Thin-layer N-S Results on a Mixed Compression Inlet (Ref. 12)	14
2-6a	A 3-D Shock-Boundary Layer Interaction Application (Ref. 13)	15
2-6b	Results of Panaras and Stanewsky (Ref. 13)	15
2-7	Glancing Shock-Boundary Layer Interaction PNS Results (Ref. 15)	18
2-8	Incident Shock-Boundary Layer Interaction with Bleed (Ref. 16)	19
2-9	P8 Application Using PPNS (Ref. 14)	20
2-10	Mixed Compression Inlet Design Analysis Using 3-D Euler (Ref.17)	21
2-11	Euler Inlet Design Application (Ref. 18)	21
2-12	Euler Analysis of Inlet Duct Hammershock Event (Ref. 19)	24
4-1	Bleed Slot Calculations (Ref. 43)	30
4-2	Incident Shock-Boundary Layer Interaction with Bleed (Ref. 25)	30
4-3	Gridding Techniques for Diffuser Exit Boundaries	35
4-4	Mixed Compression Inlet with Computational Nozzle Exit Boundary (Ref. 42)	35
5-1	Sharp Lip Extinsion on the P8 for Grid Simplification (Ref. 29)	38
5-2	Turbulent Boundary Layer Nomenclature (Ref. 3)	38
6-1	Baldwin-Lomax Model F Function Peaks in a Separated Region (Ref. 23)	44
6-2	Wall Normal Distances for Turbulence Model Applications in Multi-wall Configurations	44
6-3	Buleev Length Scale, Equation 6.14	45

1.0 INTRODUCTION

The Airframe Propulsion and Weapons Integration Section of Wright Laboratory is in the process of expanding its computational fluid dynamics (CFD) capabilities. The charter of the Section with regard to CFD and propulsion is the application of existing CFD tools on advanced inlet and nozzle components for purposes of analysis, evaluation, and design. Recent progress in applications on various nozzle configurations has been very promising, and a certain level of expertise has been achieved. However, application to high speed inlet components has not progressed to the same level. Lack of experience with such problems has led to limited success and is the primary reason for slow progress.

An extensive literature search was conducted for CFD applications to high speed inlets and inlet related flowfields. The range of materials collected include two-dimensional inviscid calculations of "unit" problems (compression ramps, shock wave-boundary layer interactions, etc.) to three-dimensional fully turbulent Navier-Stokes analyses of real inlet test hardware. This information dates back to the mid 1970's, when the first numerical solutions for supersonic turbulent flows with shock-boundary layer interactions were being obtained.^{1,2} The range of numerical applications which have been reviewed is shown in Fig 1-1. Applications to purely axisymmetric inlet configurations were excluded from the literature search. The majority of the literature covers applications in the Mach range 2-7, with a few cases for Mach number greater than 12. The altitude range where these inlets are operating as part of an airbreathing propulsion system is generally below 150,000 feet. The expected flow condition for this regime is a real gas continuum. Elevated temperatures in stagnation regions and boundary layers support the possibility of vibrational and chemical equilibrium thermodynamics. However, finite rate chemical reactions are usually not considered for inlet flows. High flight Reynolds number combined with shock wave induced disturbances guarantee that turbulent boundary layers predominate the viscous interactions. In some wind tunnel environments where Reynolds number is relatively low with an isolated inlet installation, laminar boundary layers may extend a significant distance aft of leading edges. Boundary layer transition is observed to occur in such cases.

The purpose of this report is to review important aspects of CFD application to high speed inlets and inlet related flowfields based on the data in the literature search. Topics which are covered include governing equations, numerical integration algorithms, grid requirements, numerical boundary conditions, and turbulence models. When possible, the results of numerical analyses compared to experimental data are shown to allow an assessment of the CFD application.




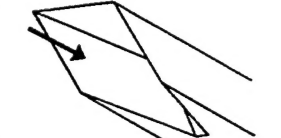


Configuration	Features		Euler	PNS	N-S
Hypersonic Mixed Compression Inlet 	<ul style="list-style-type: none"> • Mach 6 - 18 • no bleed • supersonic exit 	2 D	1	4	6
		3 D		4	5
Supersonic Mixed Compression Inlet 	<ul style="list-style-type: none"> • Mach 2.5 - 5 • bleed (porous, slot) • supersonic or subsonic exit • steady or unsteady 	2 D	5		5
		3 D	1	1	8
Supersonic External Compression Inlet 	<ul style="list-style-type: none"> • Mach 2.5 • bleed (porous, slot) • subsonic spillage • steady or unsteady 	2 D	1		4
		3 D			1
3-D Scramjet Inlet 	<ul style="list-style-type: none"> • Mach 3-5 • sidewall compression • multi-strut 	2 D			
		3 D			2
2-D Shock Wave/ Boundary Layer Interaction 	<ul style="list-style-type: none"> • Mach 1.1-3 • compression ramps • impinging shocks • normal shocks 	2 D		1	14
		3 D			
3-D Shock Wave/ Boundary Layer Interaction 	<ul style="list-style-type: none"> • Mach 3 • wedge fin on flat plate • swept compression ramp 	2 D			
		3 D			5

Figure 1-1 Survey Applications

2.0 GOVERNING EQUATIONS

The application of CFD techniques to any aerodynamic problem starts with the identification of the governing equations of the fluid motion. As mentioned in the introduction, high speed inlets operate in the compressible flow regime usually at flight Reynolds numbers which result in turbulent flow. The most general and applicable equations which govern this flow are the time dependent Reynolds averaged compressible Navier-Stokes equations. For Cartesian velocity components (u,v,w), the Navier-Stokes equations are written in strong conservation law form as

$$\frac{\partial \mathbf{U}}{\partial t} + \frac{\partial \mathbf{E}}{\partial x} + \frac{\partial \mathbf{F}}{\partial y} + \frac{\partial \mathbf{G}}{\partial z} = 0. \quad 2.1$$

The conservation variable vector is $\mathbf{U} = (\rho, \rho u, \rho v, \rho w, E_t)^T$, and the flux vectors are

$$\begin{aligned} \mathbf{E} &= \begin{bmatrix} \rho u \\ \rho u^2 + p - \tau_{xx} \\ \rho uv - \tau_{xy} \\ \rho uw - \tau_{xz} \\ (E_t + p)u - u\tau_{xx} - v\tau_{xy} - w\tau_{xz} + Q_x \end{bmatrix}, \\ \mathbf{F} &= \begin{bmatrix} \rho v \\ \rho uv - \tau_{yx} \\ \rho v^2 + p - \tau_{yy} \\ \rho vw - \tau_{yz} \\ (E_t + p)v - u\tau_{yx} - v\tau_{yy} - w\tau_{yz} + Q_y \end{bmatrix}, \\ \mathbf{G} &= \begin{bmatrix} \rho w \\ \rho uw - \tau_{zx} \\ \rho vw - \tau_{zy} \\ \rho w^2 + p - \tau_{zz} \\ (E_t + p)w - u\tau_{zx} - v\tau_{zy} - w\tau_{zz} + Q_z \end{bmatrix}, \end{aligned} \quad 2.2$$

$$E_t = \rho \left(e + \frac{u^2 + v^2 + w^2}{2} \right).$$

The viscous stress terms are

$$\begin{aligned}
 \tau_{xx} &= \frac{2}{3} (\mu + \mu_t) \left(2 \frac{\partial u}{\partial x} - \frac{\partial v}{\partial y} - \frac{\partial w}{\partial z} \right) , \\
 \tau_{yy} &= \frac{2}{3} (\mu + \mu_t) \left(2 \frac{\partial v}{\partial y} - \frac{\partial u}{\partial x} - \frac{\partial w}{\partial z} \right) , \\
 \tau_{zz} &= \frac{2}{3} (\mu + \mu_t) \left(2 \frac{\partial w}{\partial z} - \frac{\partial u}{\partial x} - \frac{\partial v}{\partial y} \right) , \\
 \tau_{xy} &= \tau_{yx} = (\mu + \mu_t) \left(\frac{\partial u}{\partial y} + \frac{\partial v}{\partial x} \right) , \\
 \tau_{xz} &= \tau_{zx} = (\mu + \mu_t) \left(\frac{\partial w}{\partial x} + \frac{\partial u}{\partial z} \right) , \\
 \tau_{yz} &= \tau_{zy} = (\mu + \mu_t) \left(\frac{\partial v}{\partial z} + \frac{\partial w}{\partial y} \right) ,
 \end{aligned}
 \tag{2.3}$$

and the heat flux terms are

$$\begin{aligned}
 q_x &= -(k + k_t) \frac{\partial T}{\partial x} , \\
 q_y &= -(k + k_t) \frac{\partial T}{\partial y} , \\
 q_z &= -(k + k_t) \frac{\partial T}{\partial z} .
 \end{aligned}
 \tag{2.4}$$

In deriving the viscous stresses, it is assumed that the turbulent stresses are proportional to the mean flow strain rates in the same manner as molecular viscous stresses. This is referred to as the Boussinesq assumption, and is discussed in more detail in Section 2.2. This set of differential equations are of course based on the conservation principles of mass, momentum, and energy. Their integration in time and/or space via numerical methods is the basic objective of CFD.

In order to make the Navier-Stokes equations tractable for numerical integration, they are usually non-dimensionalized and transformed for a uniformly spaced computational coordinate system. The transformation is pictured graphically in Figure 2-1. See Reference 3 for a complete development of this process. The transformation simplifies the discretization process and allows the digital computer program (or "code") to systematically store and retrieve the necessary information quickly. The disadvantage is the requirement to produce a highly structured field grid which can be a time consuming interactive endeavor.

2.1 Gas Properties

In addition to Equations 2.1 through 2.4, the gas state relationships between the thermodynamic variables (p, ρ, T, e, h) are needed as well as the variation of the molecular transport

properties (μ, k) with temperature. The complexity of these relationships depends upon the gas temperature range of the flows being considered.

At the pressures and temperatures expected in inlet flows, air behaves according to the perfect gas law:

$$p = \rho RT \quad 2.5$$

where R is the gas constant, which depends upon the gas composition.

For low temperatures (3K-800K), air is also considered calorically perfect, where the specific heat capacities at constant volume and pressure (c_v and c_p) are constant.⁴ A calorically perfect gas implies all of the following:

$$e = c_v T, \quad h = c_p T, \quad \frac{c_p}{c_v} = \gamma, \quad c_p - c_v = R, \quad c_v = \frac{R}{\gamma - 1}, \quad c_p = \frac{\gamma R}{\gamma - 1} \quad 2.6a$$

The values of c_v , c_p , R , and γ are all constant under the calorically perfect gas law.

As air temperature increases above about 800K, diatomic air molecules become vibrationally excited. In this case, the specific heat capacities are not constant, but functions of temperature:

$$\begin{aligned} c_v &= c_v(T) \\ c_p &= c_p(T) \end{aligned} \quad 2.6b$$

Hence, e and h are related to temperature through:

$$\begin{aligned} de &= c_v dT \\ dh &= c_p dT \\ e &= e(T) \\ h &= h(T) \end{aligned} \quad 2.6c$$

A gas is considered thermally perfect if it is not chemically reacting and the internal energy and enthalpy are functions of temperature only. The gas constant R remains unchanged.

The molecular viscosity μ is a function of temperature only for low density fluids such as air, and is normally determined from kinetic molecular theory and empiricism.⁵ One relation is the well known Sutherland's law,

$$\frac{\mu}{\mu_0} = \left(\frac{T}{T_0} \right)^{3/2} \frac{T_0 + S}{T + S} \quad 2.7a$$

where the subscripted quantities are reference values and S is a constant. Sutherland's law is accurate for air to within 2% in the temperature range 170K-1900K. The power law,

$$\frac{\mu}{\mu_0} = \left(\frac{T}{T_0} \right)^n, \quad n \approx 0.7 \quad 2.7b$$

is slightly less accurate (4%) over the same temperature range.⁵ Of the applications investigated here which disclosed the particular viscosity relation used, all but one used Sutherland's law. Agarwal, Deese, and Peters⁶ is the one exception which used the simpler power law. No particular reason is given for their selection. It is doubtful that one could identify any difference in inlet CFD solutions obtained with these different molecular viscosity relations, especially since turbulence dominates the viscous phenomena anyway. The fact that many of the application references do not even disclose which relation is used is further evidence that the selection is not critical. The one advantage the power law has is that it can be completely non-dimensionalized; Sutherland's law requires a characteristic temperature value for non-dimensionalization.

The thermal conductivity k is also a function of temperature, but can be related to molecular viscosity via the Prandtl number:

$$Pr = \frac{\mu C_p}{k} \quad 2.8$$

where the Prandtl number is assumed to be constant. The Prandtl number was 0.72 (air at standard conditions) for most of the applications reviewed for this report. A value of 0.73 was used in a few applications. None of the references discuss the impact of choosing one value over the other; the result would be on the order of one percent difference in thermal conductivity. Again, it is unlikely that any difference could be discerned in inlet solutions.

At higher Mach numbers, temperatures at stagnation points and in boundary layers may be high enough to cause molecular dissociation and other chemical reactions (at atmospheric pressure, O_2 dissociates at 2000K and N_2 dissociates at 4000K).⁴ These are energy absorbing processes. Under these conditions, the specific heat capacities are functions of temperature and pressure and the gas chemical composition can change. A high temperature gas model is used for the gas state relations and the transport coefficients. These models are called equilibrium air models. They return the experimentally observed equilibrium state of the gas as a function of temperature and pressure. The molecular transport coefficients are also determined as a function of temperature. Equilibrium air models are generally empirical curve fits or table look-up routines, and as such require more computing resources than the simple algebraic expressions of the perfect gas law and calorically perfect gas relationships. None of the applications reviewed here considered non-equilibrium chemistry. It is usually assumed that the chemical reactions are fast compared to the inlet flow residence time. Finite rate chemistry gas models do exist, however, and are often used for hypersonic nozzle flows.

References 7, 8, and 9 have studied the effects of different values of γ in perfect gas calculations as well as full equilibrium air models on the NASA P8 inlet model.¹⁰ This model, shown in Figure 2-2, was tested at Mach 7.4 and continues to be a favorite subject of CFD application. The freestream conditions were air at Mach 7.4, Reynolds number of 8.86 million per meter, and total temperature of 811K. The model is a mixed compression fixed geometry inlet for scramjet propulsion. The design incorporates a single external ramp shock, and a cowl

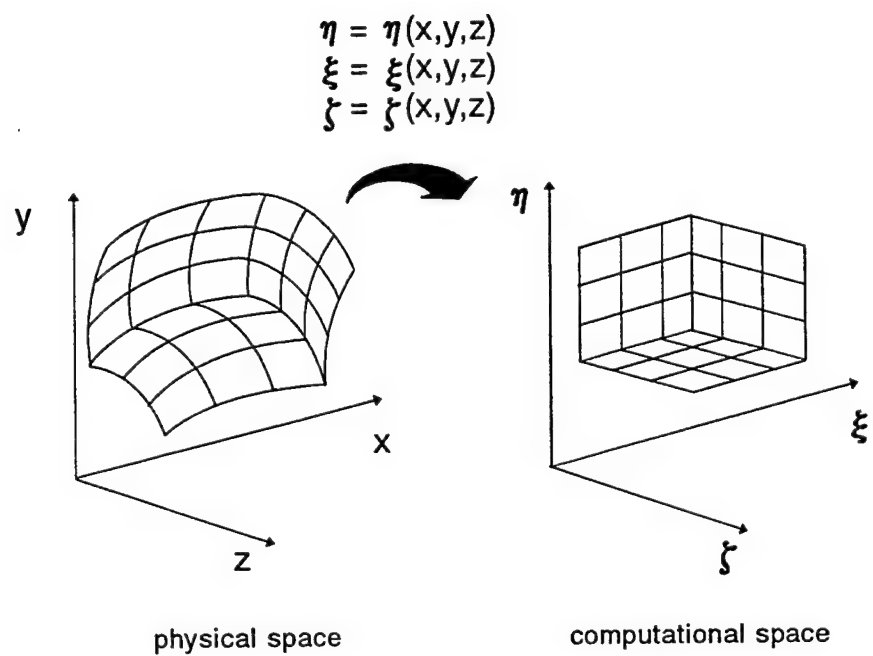


Figure 2-1 Coordinate Transformation Schematic

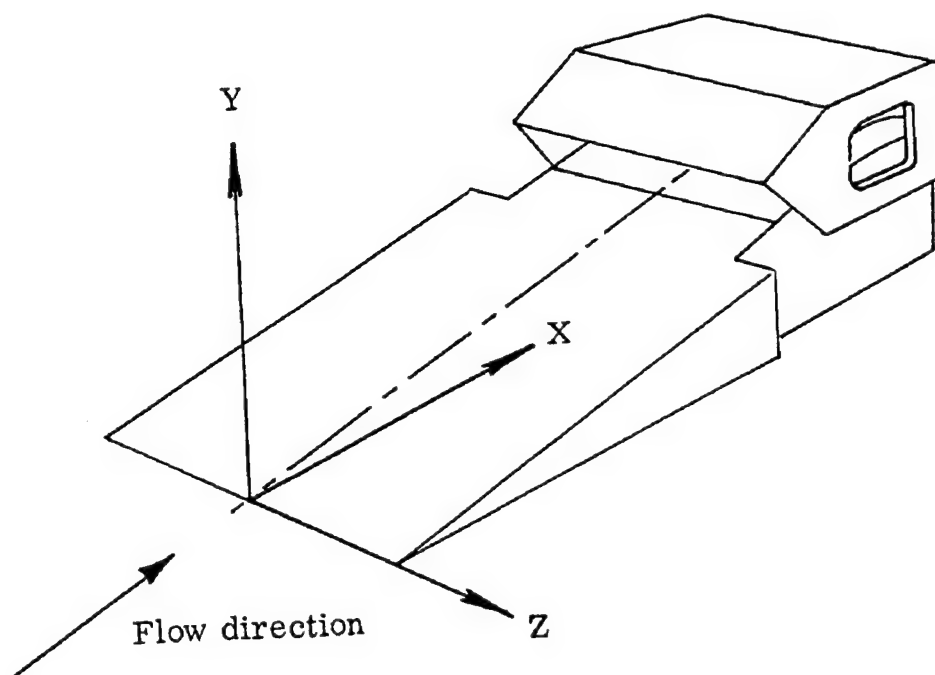


Figure 2-2 NASA P8 Inlet (Ref. 10)

shock which reflects weakly off the ramp shoulder. No boundary layer separation was observed at this interaction. Instrumentation was primarily to map to the flowfield, rather than measure performance. Wall static pressure and temperature distributions were taken on the ramp and cowl. Also pitot pressure and total temperature vertical surveys from ramp to cowl were taken at many streamwise stations throughout the model. Successfulness of CFD applications to the P8 has generally been based upon comparison to the pitot pressure profiles.

For CFD analysis, Mach 7.4 is high enough to warrant the use of high temperature gas properties. However, the freestream total temperature of the wind tunnel was well below flight conditions, which lead the authors of these references to compare numerical results using perfect gas versus high temperature gas models.

Kunik, Benson, Ng, and Taylor⁷ compared values on the P8 inlet for γ of 1.4 and 1.38 in perfect gas calculations. The technique of using $\gamma < 1.4$ with a perfect gas model is a convenient way to investigate first order effects of high temperature without the complexity of the full equilibrium air model. They concluded that there were significant differences in the pitot pressures obtained and in the location of the shock waves, as would be expected. Their results show that the pitot pressures for $\gamma = 1.38$ are much closer to the experimental data as compared to the $\gamma=1.4$ results. (The results are not shown here due to poor quality of the reference copy.)

Rhie and Stowers⁸ compared results on the P8 inlet for a perfect gas model with $\gamma = 1.38$ to an equilibrium air model. They concluded that the equilibrium air model did not show any significant difference as compared to the perfect gas with $\gamma = 1.38$. They did not perform calculations with $\gamma = 1.4$.

Brenneis and Wanie⁹ performed calculations on the P8 inlet with perfect gas using $\gamma = 1.4$ and 1.38 and also an equilibrium air model. The $\gamma = 1.38$ perfect gas calculation matched the experimental pitot pressure profiles best overall as shown in Figure 2-3. Note that all three calculations are significantly different from each other, indicating that the pitot pressure is very sensitive to changes in γ . In contrast, the authors mention that the wall static pressure distributions were not affected by the gas models. The authors conclude that high temperature gas effects are present in their solutions. They suggest that to fully compare the CFD results to test data, the CFD solution would have to include the flow about each pitot probe. (Incidentally, the equilibrium air calculation took 20% more CPU time than the perfect gas calculations.)

Note that Brenneis and Wanie observed a difference in their results between $\gamma=1.38$ and the equilibrium gas model, while Rhie and Stowers found no significant difference. The equilibrium air models used in these separate references are from different sources, which might explain the conflicting conclusions.

It is obvious from the above discussion that high temperature gas effects are first order for the P8 inlet test, even at the low freestream stagnation temperature. As a general rule of thumb, high temperature gas models probably should be considered for inlet calculations above a Mach number of about 6.

2.2 Time Averaged Turbulent Stress and Heat Transfer

The turbulent viscosity (or eddy viscosity) coefficient μ_t in Equation 2.3 is a result of two important developments of the unsteady Navier-Stokes equations. First, it is assumed that flow variables in a turbulent flow can be decomposed into a time averaged mean plus a fluctuating

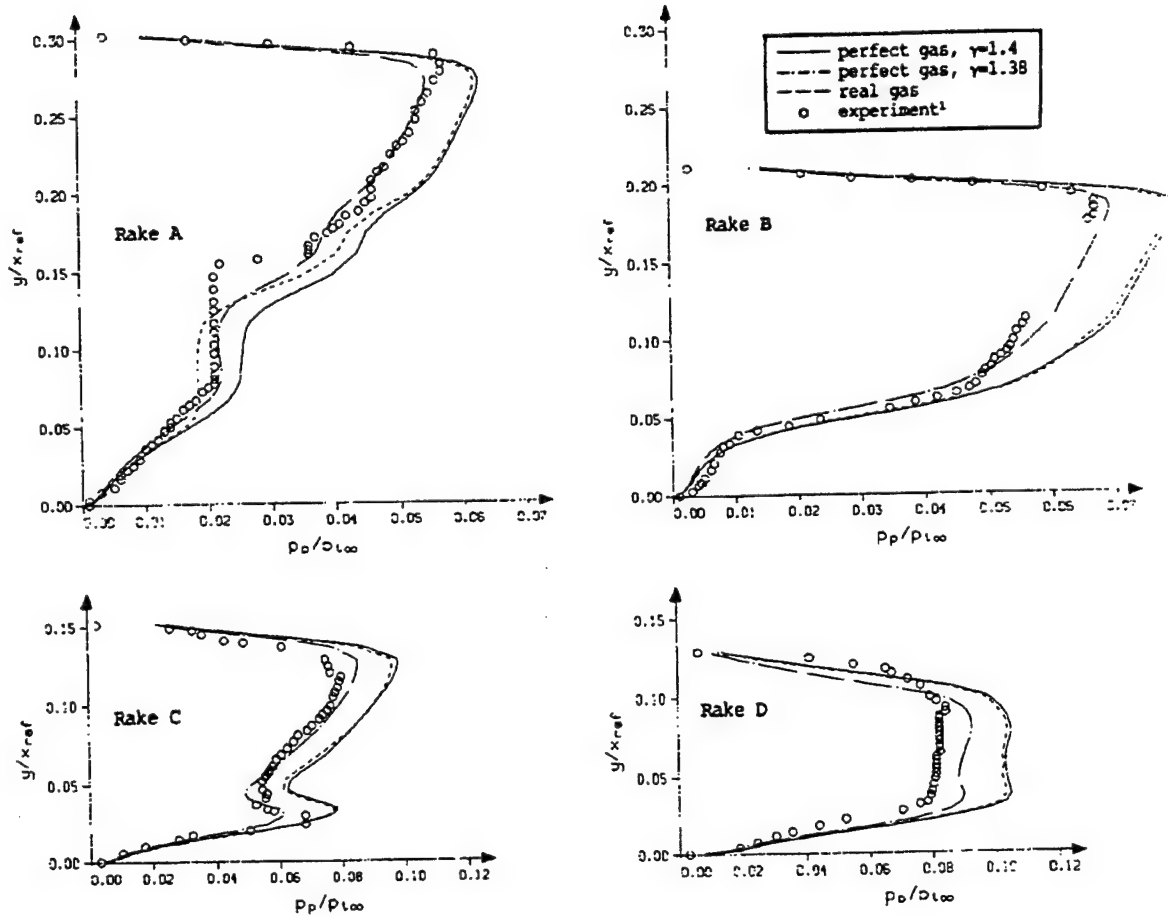


Figure 2-3 P8 Calculations with High Temperature Gas Models (Ref. 9)

component:

$$\phi = \bar{\phi} + \phi', \quad \bar{\phi} = \frac{1}{\Delta t} \int_{t_0}^{t_0 + \Delta t} \phi dt \quad 2.9$$

where ϕ could be any of the flow variables. The time increment Δt is large compared to the fluctuations, but relatively small compared to the time constant of any unsteadiness in the mean flow. This is depicted in Figure 2-4. The decomposed flow variables are substituted into the governing equations which are then time averaged. In this process, most of the fluctuating terms drop out by definition of the time average or are neglected. The extra terms that remain are due to correlations of the fluctuating velocity components. See Reference 3 for the details of this derivation. These terms are referred to as apparent turbulent stresses. Second, to cast the equations in the form given in Equations 2.1-2.4, it is further assumed that the apparent turbulent stresses are proportional to the mean flow strain rates through the turbulent eddy viscosity coefficient. This is called the Boussinesq assumption and is made by every reference dealing with turbulent flow reviewed herein.

The turbulent coefficient of thermal conductivity, k_t , in the energy equation is also a result of the same developments discussed above. The apparent turbulent heat flux is a result of correlations of the fluctuating velocity components and fluctuating temperature. The Boussinesq assumption relates the apparent turbulent heat flux to the gradients of the mean temperature through the turbulent thermal conductivity coefficient. In practice, this coefficient is related to the turbulent viscosity coefficient by a turbulent Prandtl number:

$$Pr_t = \mu_t c_p / k_t \quad 2.10$$

The turbulent Prandtl number Pr_t is taken to be 0.9 for all the turbulent applications reviewed herein.

There are two different commonly used time averaging procedures for the governing equations. The first is a strict time average as shown in Equation 2.9, and is referred to as Reynolds averaging. The other is a mass-weighted time average, or Favre average, where the time mean flow variables are defined as

$$\bar{\phi} = \frac{\overline{\rho \phi}}{\bar{\rho}} \quad 2.11$$

Some authors claim advantages to mass-weighted averaging.^{3,11} The compressible turbulent Navier-Stokes equations with mass-weighted variables is nearly identical to the incompressible turbulent Navier-Stokes equations. According to Wilcox and Traci¹¹, this is consistent with a hypothesis due to Morkovin that turbulence in equilibrium behaves in a locally incompressible manner. However, flows undergoing rapid expansions or compressions are not in equilibrium with respect to turbulence. Thus compressibility corrections are needed in the turbulence closure models. Of the application references reviewed here dealing with turbulent flows, about half use mass-weighted averaging and half use Reynolds averaging. No direct comparisons were made between the two in any of the references.

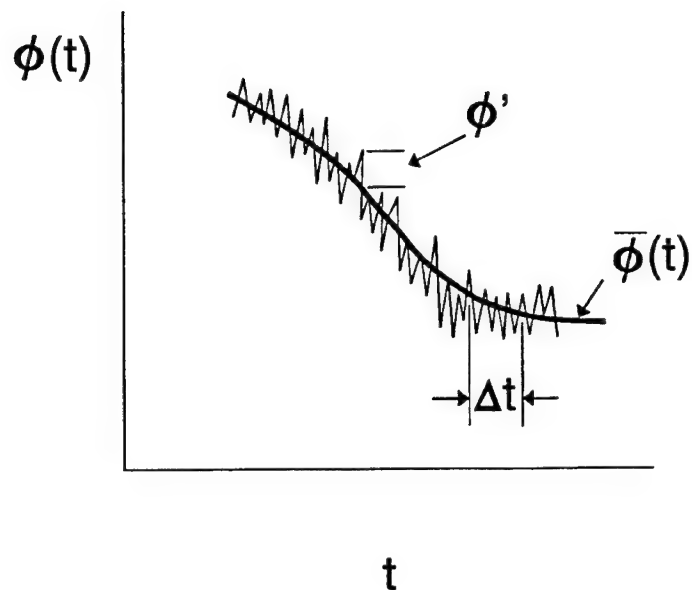
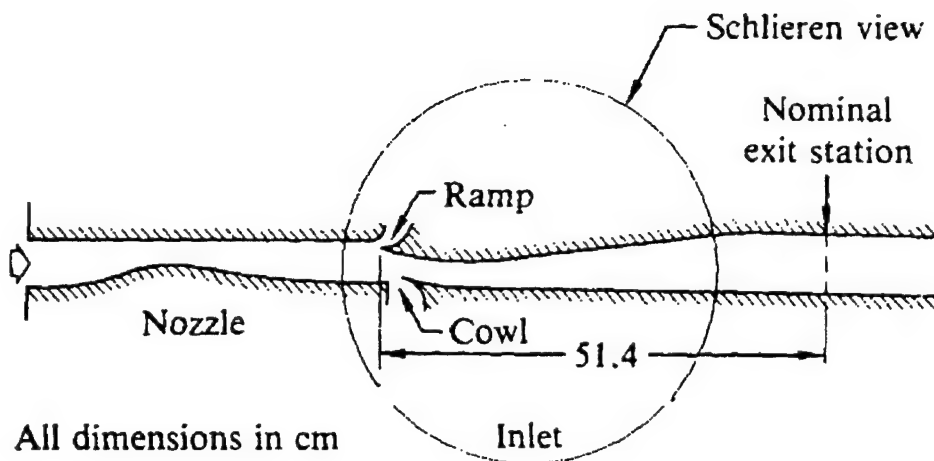


Figure 2-4 Unsteady Mean Flow with Fluctuating Components



- Aspect ratio at throat: 7.56
at exit: 2.80

Figure 2-5a Mixed Compression Inlet Application (Ref. 12)

2.3 Subsets of the Navier-Stokes Equations

The time dependent Navier-Stokes equations are a mixed set of hyperbolic-parabolic partial differential equations³ which govern flow behavior for initial-boundary value problems. They are solved by integrating in time from some initial condition to a steady state (if one exists) with influence from the boundaries of the domain of interest. It is beneficial to determine if appropriate approximations can be made to simplify the governing equations and therefore reduce computer requirements in terms of memory and processing time. A discussion of the simplified equation subsets which have been applied to high speed inlets is given below, including thin layer Navier-Stokes, parabolized Navier-Stokes, and Euler. In general, all of the problems shown in Figure 1-1 can be solved using state-of-the-art Navier-Stokes codes. This section will investigate which flows have also be successfully solved with the simplifying approximations.

2.3.1 Thin Layer Navier-Stokes

The thin layer Navier-Stokes equations are derived by neglecting viscous derivatives parallel to solid walls. The usual boundary layer order of magnitude analysis is used which retains only viscous derivatives in a direction normal to the wall. This can be accomplished easily in computational coordinates which are generally oriented with the body surfaces. The assumption is best for high Reynolds number flows where the boundary layers are expected to be thin relative to the inviscid core flow dimensions. Unlike the boundary layer equations, the thin layer equations retain all other terms in the momentum equation, which makes them applicable to separated and reverse flows as well. Note also that the thin layer approximation neglects both molecular viscous stresses and turbulent Reynolds stresses in the streamwise direction.⁶ The advantage over the full Navier-Stokes equations is a reduction in the number of terms needing to be evaluated by the computer and thus reduced CPU time. The character of the equations has not been changed, so integration in time is still required for a solution. The thin layer Navier-Stokes equations appear to be attractive for high speed inlets operating in a high Reynolds number environment. However, one might question the ability of this set of equations to capture the complex viscous phenomena of shock wave-boundary layer interactions, shock induced separations, etc., which are typically found in inlet flows.

Agarwal, Deese, and Peters⁶ have carefully applied a thin layer, mass-averaged code to a variety of shock wave-boundary layer interactions, including 2-D and 3-D, separated and unseparated flows. The primary objective of their work was to study the role of turbulence closure models in such flows. However, they show through order of magnitude analysis that the thin layer approximation is appropriate even for strong interactions (separated flows) when the separation bubble is "small." In general, their results show the same discrepancies to experimental data as full Navier-Stokes applications of the same flows. Their concluding remarks indicate that the thin layer approximation is not affecting the results; the reason for discrepancies is attributed to turbulence models (see Section 6.0).

Liou, Hankey, and Mace¹² have applied a thin layer Reynolds-averaged code to a 2-D supersonic mixed compression inlet (Figure 2-5a). The computed flow exhibits all the prominent features observed in the test, including shock induced separation, and the natural unsteadiness of the terminal shock in the diverging channel. Comparisons to experimental data show the same

reasonable agreement as full Navier-Stokes calculations of other mixed compression inlets (Figure 2-5b). Again, the reason for discrepancies is not attributed to the thin layer approximation.

Panaras and Stanewsky¹³ have applied a thin layer code to a fin generated 3-D shock wave-boundary layer interaction. No discussion is given for the suitability of the thin layer approximation to this type of flow, except that it has been applied to other supersonic corner flows. Their results capture even the fine details of the flow observed in the corresponding experiment, as shown in Figures 2-6a and 2-6b. The success of their results is attributed to a turbulence model which is finely tuned to this type of flow.

Unfortunately, none of the applications show a direct comparison of thin layer approximation to full Navier-Stokes results. Also, the authors discussed above did not indicate how much computer resources were saved by using the thin layer approximation. It appears from the above discussion that the thin layer approximation can be applied successfully to high speed inlet flows, provided the flow separations are not too severe.

2.3.2 Parabolized Navier-Stokes

The Parabolized Navier-Stokes (PNS) equations are derived by neglecting streamwise derivatives in the viscous terms of the *steady* Navier-Stokes equations. With a restriction to supersonic inviscid core flow, the governing equations reduce to a set which is parabolic in the streamwise direction. A solution to the PNS equations then becomes an initial-boundary value problem which is integrated by marching in space rather than time. An order of magnitude analysis³ shows that the exclusion of the streamwise viscous terms only becomes appropriate for hypersonic flows when the freestream Mach number is about five or higher. The exclusion of these terms eliminates the ability to compute streamwise separations, although crossflow separations can still be predicted since all crossflow terms are retained.

Theoretically, steady hypersonic flow can be completely solved in one sweep of the streamwise direction, including fully coupled inviscid and viscous interactions. Furthermore, only the solution at the current marching step is stored in core memory, not the entire flow domain. This has obvious major savings in computer processing time. For these reasons, a larger number of grid points can be used to resolve the boundary layer than for full Navier-Stokes calculations. To start a PNS solution, the flow field must be known completely at some initial station from which the streamwise marching begins. This can be the freestream for configurations with sharp leading edges, or a Navier-Stokes solution for a blunt leading edge.

Strictly speaking, the streamwise space marching integration assumes no upstream influence and thus requires the inviscid flow to be supersonic with no negative velocity components, i.e., no separation. However, any streamwise pressure gradients will exhibit upstream influence through the subsonic portion of the boundary layer. This causes the numerical problem to be ill-posed and will result in unstable "departure solutions" unless approximations are made to the pressure gradient term. The sublayer approximation assumes that the streamwise pressure gradient is nearly constant across the boundary layer in high Reynolds number flows, and thus can be evaluated in whole or in part in the supersonic region of the boundary layer. Other PNS codes¹⁴ use a multi-pass technique which uses the results of one streamwise sweep to estimate the streamwise pressure gradient for the subsequent sweep. The sweeps continue until no changes are seen. This process is sometimes referred to as global pressure relaxation. Still,

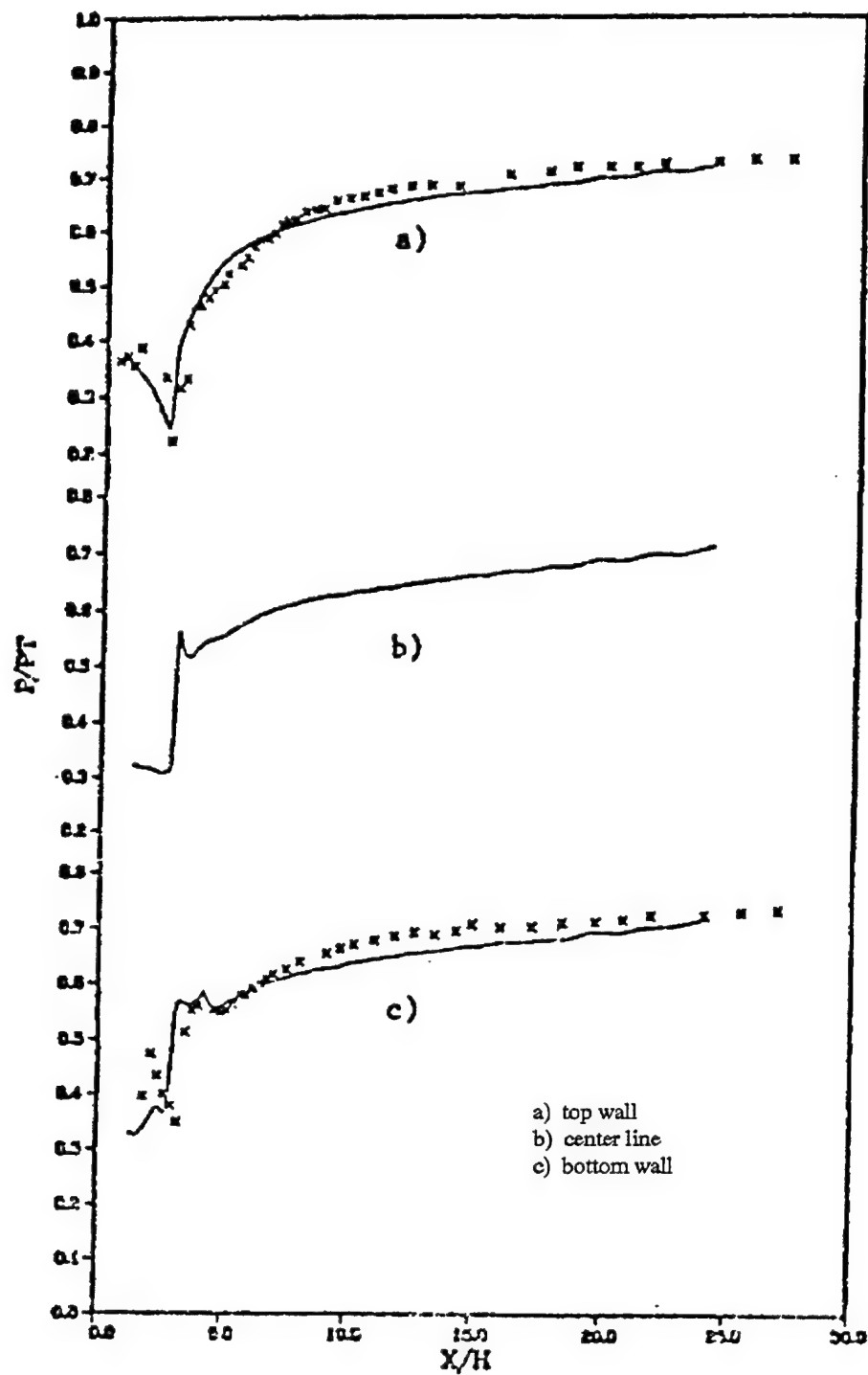


Figure 2-5b Thin-layer N-S Results on a Mixed Compression Inlet(Ref. 12)

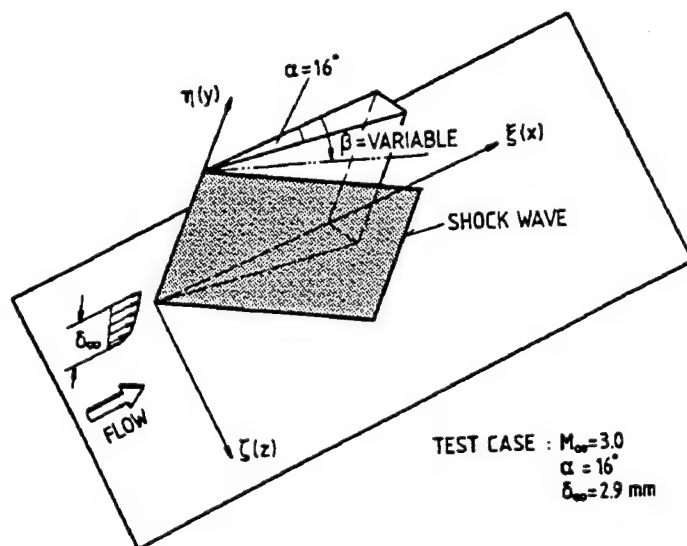


Figure 2-6a A 3-d Shock-Boundary Layer Interaction Application (Ref. 13)

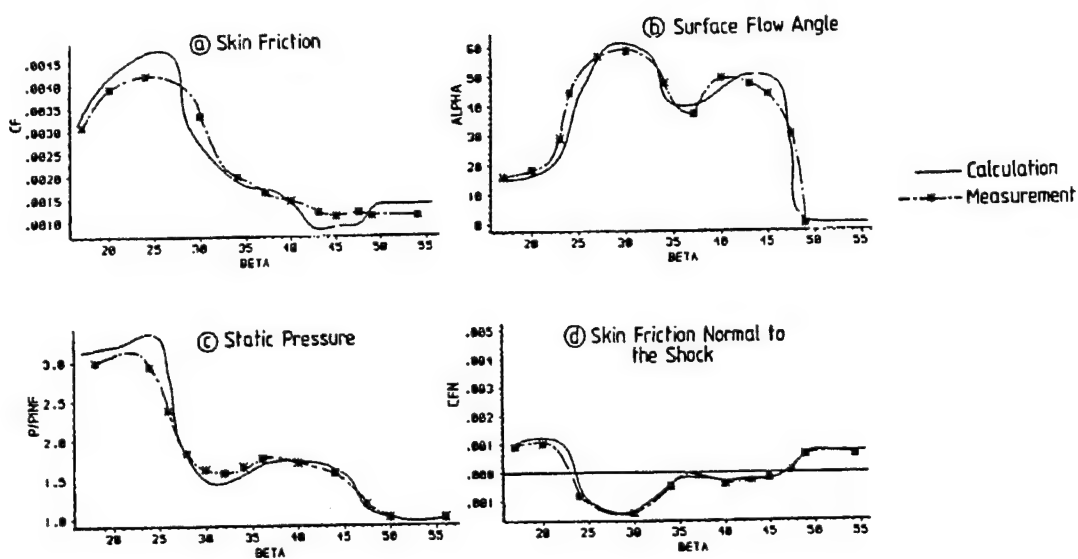


Figure 2-6b Results of Panaras and Stanewsky (Ref. 13)

the total processing time for a PNS solution is much less than a time integrated full Navier-Stokes solution.

Applications of the PNS equations to high speed inlet flows are numerous, primarily because of the comparative ease with which solutions can be obtained. Researchers at NASA Lewis have used their PNS code for the P8 inlet in two and three dimensions, 3-D glancing shock-boundary layer interactions, and other mixed compression inlets (limited to the supersonic portion only). These applications are discussed below.

Kunik, Benson, Ng, and Taylor⁷ comment that PNS analysis of mixed compression inlets may be appropriate because viscous phenomena which cannot be solved by PNS (i.e., separation) would lead to unstarts and poor design anyway. They conclude that it is necessary from a design standpoint to predict the onset of separation, but not the details of separated flow. They used 2-D PNS analysis to study effects of grid spacing, turbulence models, and high temperature on the P8 inlet. Because the solutions were quickly obtained, an optimization of these parameters could be performed. As described earlier, they were able to obtain good agreement with the pitot pressure profiles. A 3-D PNS calculation was also performed, but a good comparison to experiment cannot be made since the P8 test model was not sufficiently instrumented for 3-D features. The CFD results do show a substantial amount of three-dimensionality created by the cowl shock interaction with the sidewall (not shown due to poor quality original).

In Reference 15, an AGARD working group was tasked to determine the current capabilities of CFD applications from participating US and European agencies on several inlet related test cases. The NASA Lewis researchers applied their PNS code to the fin generated glancing shock-boundary layer interaction test case and the P8 inlet again. The results were compared with test data and a number of full Navier-Stokes calculations from the various agencies. Very little details of the applications were given; the focus was on the results and comparisons. The PNS code used in Reference 15 was the same as the one used by Kunik et al.⁷

For the 3-D glancing shock-boundary layer interaction, the PNS code was able to predict qualitatively the features of the interaction. Figure 2-7 shows the wall pressure comparisons with experiment and several other Navier-Stokes calculations. The PNS code exhibits the correct amount of upstream influence, as shown by the initial pressure rise at $y=3$. However, the pressure in the plateau region is over predicted. The fact that the PNS code can predict the upstream influence is a consequence of this type of flow, not the PNS method. The ellipticity of the 3-D glancing shock wave-boundary layer interaction acts mostly in a spanwise direction, and the 3-D PNS equations retain all of the spanwise terms as noted previously. Note that even the Navier-Stokes calculations have discrepancies in one or more regions of the wall pressure plot. The pitot pressure profiles and a yaw angle profiles shown in Reference 15 illustrate that the PNS code does as well as the full Navier-Stokes codes for these parameters. The conclusion for this case in Reference 15 is that all the CFD analyses (including NASA Lewis' PNS) were applicable to this type of flow, but that user involvement in modeling decisions (turbulence models, boundary conditions, etc.) will have a strong influence on the results.

For the P8 application in Reference 15, ten different CFD analyses were compared against each other and the test data. The plots are not shown here because the number of curves per plot makes them difficult to read. It appears that the PNS results in this reference do not agree with the test data as well as the results of Kunik et al.⁷ Again, no details of the PNS solution were

given in Reference 15. Since Kunik et al⁷ conducted a careful optimization of the parameters affecting the solution, it is concluded that their results represent the best application of NASA Lewis' PNS code to the P8 inlet.

Kim, Buggeln, and McDonald¹⁶ have applied a different "parabolized" Navier-Stokes method to a 2-D shock wave-boundary layer interaction with bleed and a 3-D rectangular inlet with spillage. The method involves identification of a primary flow direction, aligning a coordinate with that direction, and neglecting all diffusion along that coordinate. The approximation is appropriate for high Reynolds number flow. The subsonic region of the boundary layer is treated with additional approximations to continuity and the normal momentum equation based on the reasoning that the subsonic region will be thin. This has resulted in a space marching method which does not exhibit the same tendency for "departure solutions" as other PNS codes.

Their application to an incident shock wave-boundary layer interaction with bleed is shown in Figure 2-8. For this case, the upstream Mach number is only 2.5, which would usually be considered too low for PNS. Separation is avoided in this interaction by a boundary layer bleed region. The wall pressure comparisons show under prediction at both ends of the interaction, which the authors attribute partially to lack of upstream influence in the space marching procedure. It is also probable that the bleed boundary conditions have some effect, per the discussion in Section 4.2. The pitot pressures agree qualitatively with the experimental data. The authors conclude that their marching procedure is applicable to this type of flow with wall bleed. However, caution is advised here because there is much experimental data showing that shock induced separation and its control by bleed is sensitive to bleed amount and location. A situation where separation is not controlled (due to insufficient bleed rate or poor location) is an eventuality for engineering applications. In this case the PNS method may not produce a solution, or may produce an erroneous solution.

Kim, Buggeln, and McDonald¹⁶ investigated the 3-D mixed compression inlet to determine PNS applicability to inlets with significant crossflow caused by spillage and sidewall interactions. No test data was available for this case. The PNS method was shown to be capable of capturing the complicated 3-D spillage flow near the sideplate lip and the 3-D glancing shock-boundary layer interactions along the sidewalls caused by the ramp and cowl shocks.

An example of a global pressure relaxation technique is given by Yaghmaee and Roberts.¹⁴ Their method uses forward differencing of the streamwise pressure gradient to simulate ellipticity of the pressure field in the subsonic boundary layer region, with multiple streamwise sweeps to converge on a solution. This method is also sometimes referred to as partially parabolized Navier-Stokes (PPNS). The authors have applied this technique to subsonic flows, terminal normal shocks, and shock wave-boundary layer interactions in other references. Note that their implementation allows the code to switch from single pass PNS to multi-pass PPNS at user discretion. This is convenient since one can march along with PNS until a strong elliptic region is encountered and then switch to PPNS. In this reference, they have applied the technique to the P8 inlet. Some of their results are shown in Figure 2-9. They have about the same level of agreement to the test data as was shown in Reference 15. The authors concluded that application of PPNS in the shock-boundary layer interaction region did not make a significant difference for the P8 because the interactions were relatively weak.

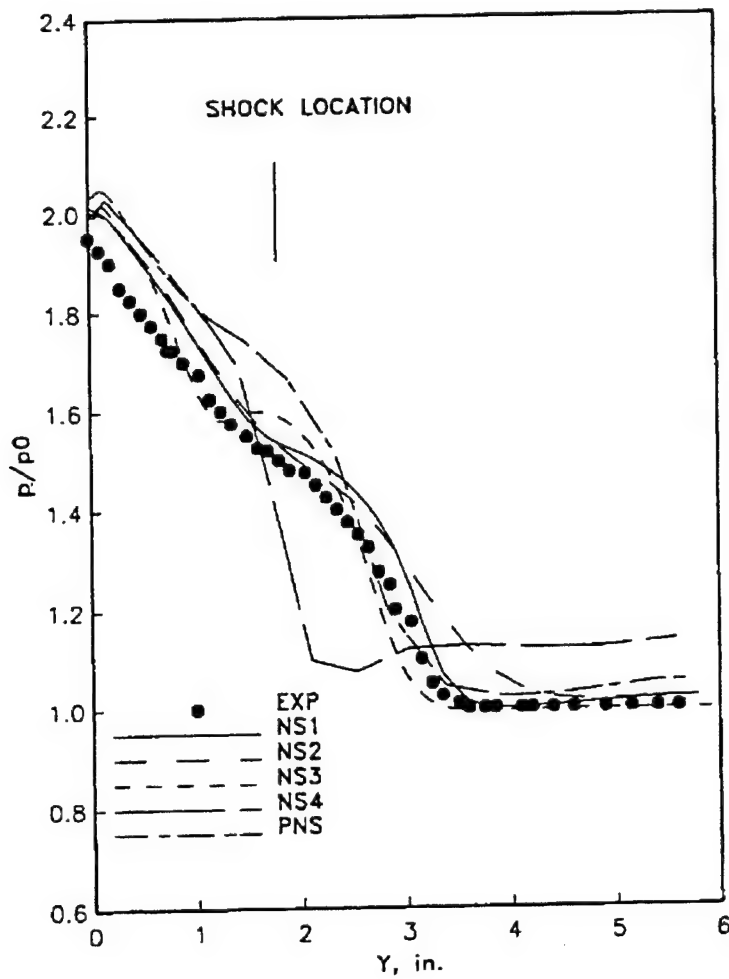
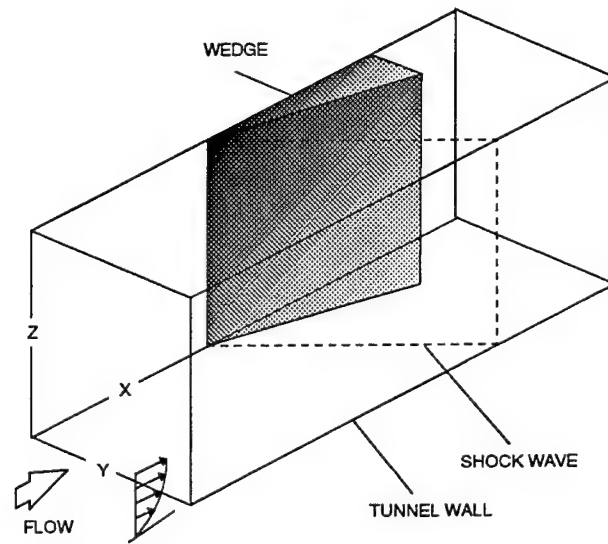


Figure 2-7 Glancing Shock-Boundary Layer Interaction PNS Results (Ref. 15)

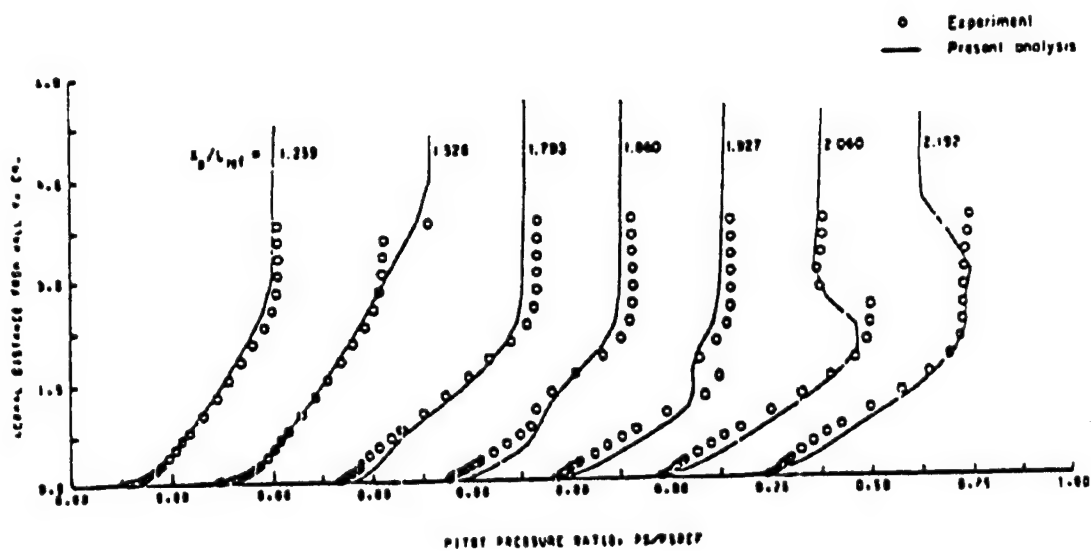
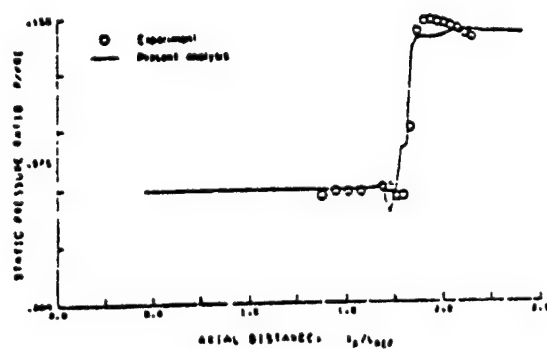
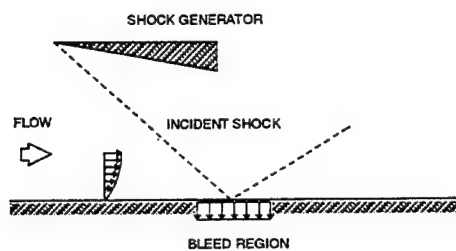


Figure 2-8 Incident Shock-Boundary Layer Interaction with Bleed (Ref. 16)

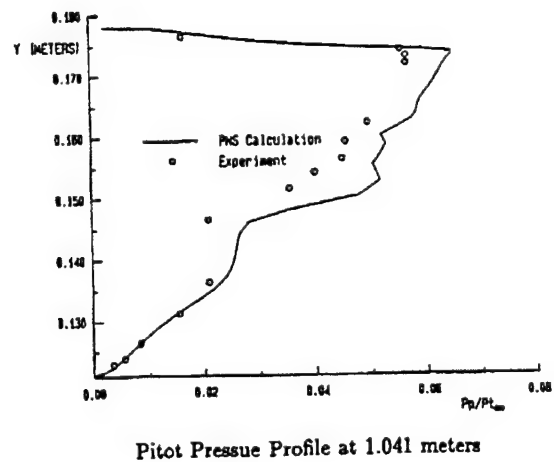
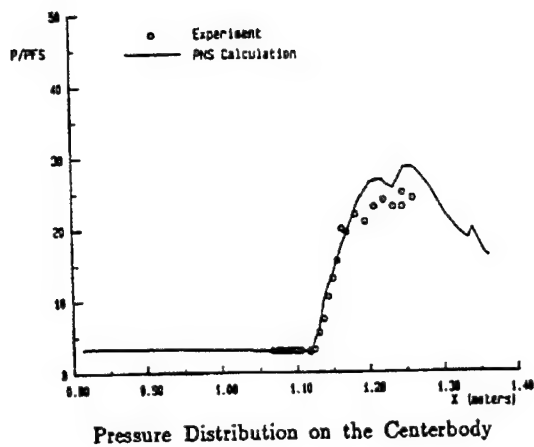
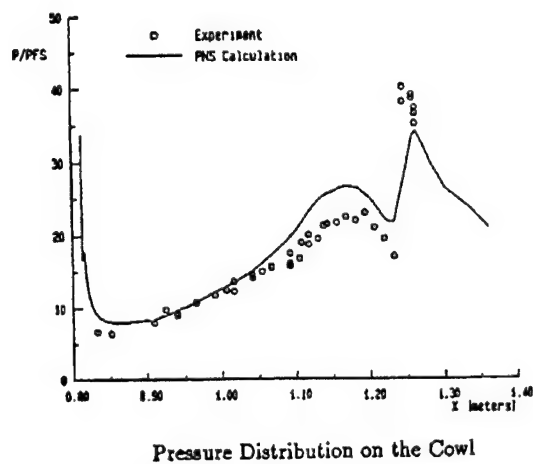


Figure 2-9 P8 Application Using PPNS (Ref. 14)

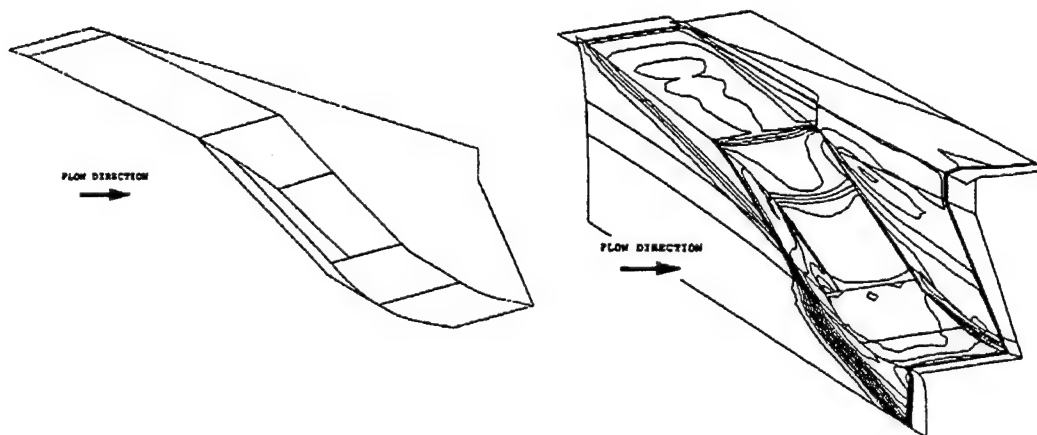
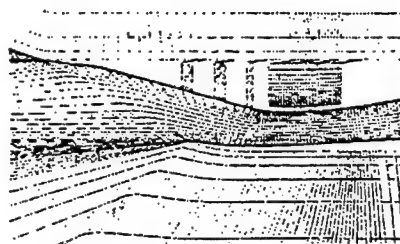
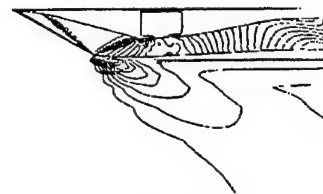


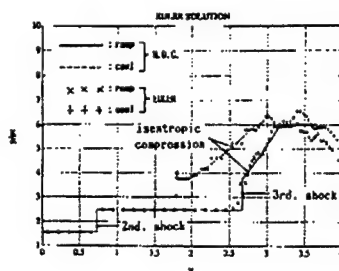
Figure 2-10 Mixed Compression Inlet Design Analysis Using 3-D Euler (Ref. 17)



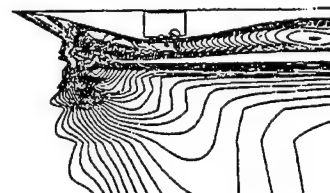
Calculation Cells.



Euler Solution.



Wall Pressure Distributions (Euler Solution).



Navier-Stokes Solution.

Figure 2-11 Euler Inlet Design Application (Ref. 18)

2.3.3 Euler Equations

The Euler equations are the inviscid subset of the unsteady Navier-Stokes equations. They have the same temporal characteristics as the Navier-Stokes equations, and so are integrated in time to yield a solution. The advantages numerically are twofold. First, all viscous terms are dropped which means fewer computer operations per time step. Second, resolution of thin boundary layers is not necessary. Boundary layer resolution involves many closely spaced grid points, resulting in a much larger number of grid points for a given flow domain than an Euler solution. The disadvantage, of course, is that important viscous phenomena and interactions are not modelled. Shock wave-boundary layer interactions are unavoidable in high speed inlets; their control is a crucial design issue and the focus of continuing research. Thus it would seem that the Euler equations have limited utility in high speed inlet applications. However, the state-of-the-art design procedure for inlets is to apply inviscid analysis to a conceptual design to determine approximate shock wave locations and strengths, pressure gradients, etc. Boundary layer displacement corrections and empirical shock wave-boundary layer interaction techniques are then applied to modify the design as necessary. The Euler equations can provide a quick, inexpensive solution for design purposes.

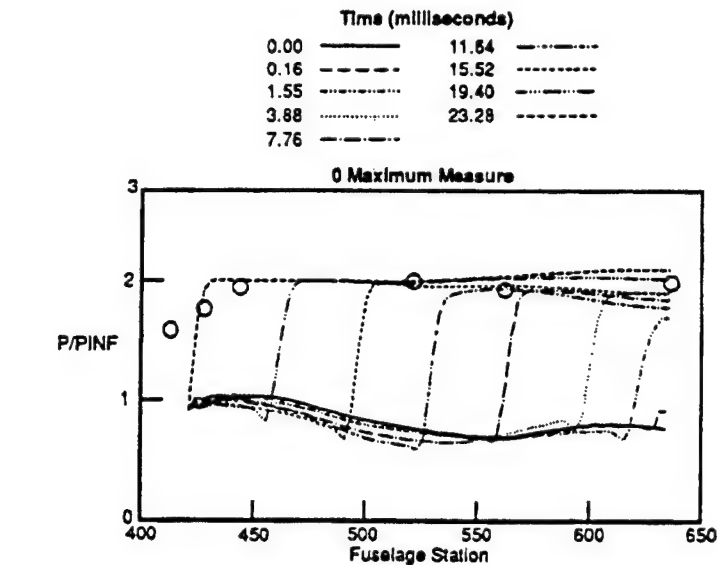
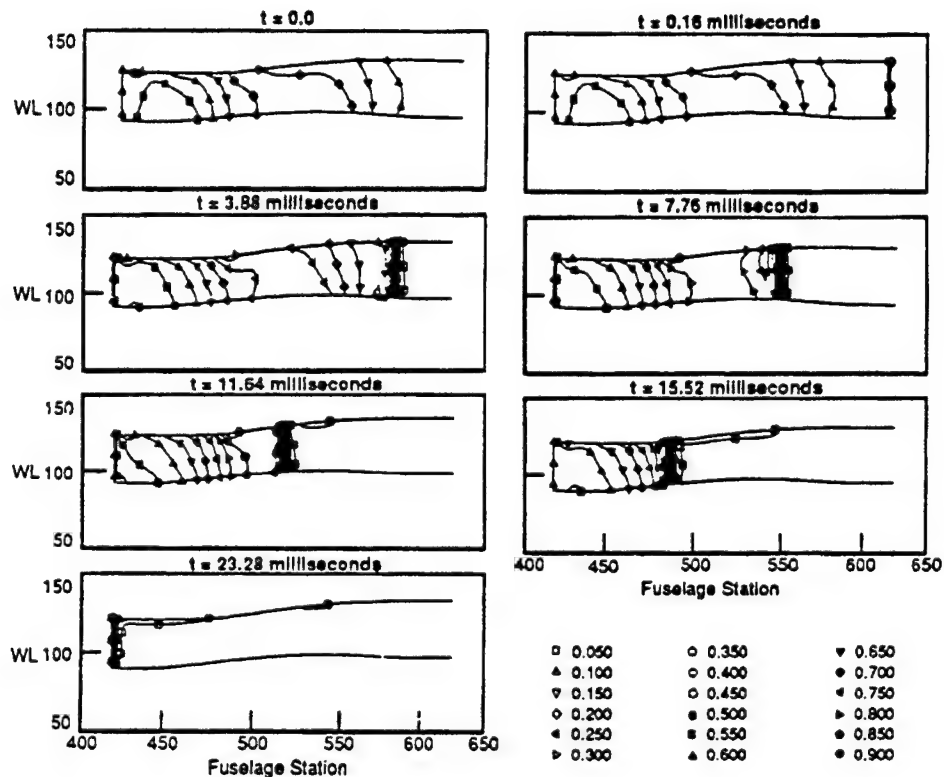
There are two examples in this review where the Euler equations have been used for inlet analysis/design. Bissinger and Eberle¹⁷ have used an Euler solver to study the flow in a Mach 5.65 mixed compression inlet, as shown in Figure 2-10. From a design standpoint, they have investigated starting enhancement by bleed, Mach number perturbations, and 3-D shock structure. The Euler analysis was capable of predicting a small subsonic pocket near the ramp shoulder which would no doubt cause an unstart in a viscous flow. Also, the 3-D solution shows the effects of the sidewalls and the resulting curvature of the ramp shocks. This type of information is needed to modify the design to avoid unstart and reduce sidewall spillage.

Fujimoto, Niwa, and Sawada¹⁸ have obtained an Euler solution on a Mach 2.5 mixed compression inlet to verify their method-of-characteristics design process. The results shown in Figure 2-11 indicate the Euler and method-of-characteristics are closely matched. However, a Navier-Stokes solution of the same configuration shows that shock induced boundary layer separation will cause unstart unless substantial bleed is used. This result illustrates the usual limitation of Euler analysis in inlet design, where viscous effects can seriously alter the expected flow patterns.

Another area where the Euler equations are useful is in the analysis of terminal shock stability and unsteady operational phenomena. Many references (17,18,19,20) attempting to solve mixed compression inlets with terminal normal shocks indicate that shock position is highly sensitive to subsonic exit boundary pressure, proximity of the exit boundary to the shock, and flow solver numerical integration parameters. These are numerical modeling issues not directly related to viscous phenomena and can be efficiently investigated with Euler analysis. Unsteady phenomena being investigated are inlet unstart, buzz, and hammer shock. These events can be triggered by shock induced boundary layer separation, freestream disturbances, or engine surge. Shock induced separation is of course a viscous phenomenon, but freestream disturbances and engine surge can occur independently of the inlet. The Euler equations are applicable because once the event is initiated, the inlet flow is dominated by inviscid transient shock wave motion. Unstart, buzz, and hammer shock events have been known to cause structural damage, and

estimates of potential inlet duct over-pressures are needed for structural design purposes.

Hindash, Bush, and Cosner¹⁹ applied the Euler equations to the classic 1-D shock tube problem to verify their accuracy for analysis ofammershock events. They found that the shock wave speed and strength (pressure rise) could be computed within 5% of the analytical solution. Further analysis of a fighter inlet ductammershock event is shown in Figure 2-12. The pressure rise along the duct is compared to flight test data where the maximum pressure at several duct locations was recorded as the shock passed forward. The computational results were found to be within 5% of the test data. The authors conclude that this is sufficient for structural design purposes.



Transient Mach Number Solutions of a 2-D Fighter Inlet During a Surge and Ramp Side Pressure Experimental Data Comparisons, Using Standard Day Properties at 20,000 Ft Altitude and $M_2 = 0.61$

Figure 2-12 Euler Analysis of Inlet Duct Hammershock Event (Ref. 19)

3.0 NUMERICAL INTEGRATION SCHEME

The focus of scheme development is the discretization and linearization of the nonlinear governing equations over small increments of time and space, and the numerical procedures used to solve the resulting algebraic system. The objective is to obtain a scheme which solves the system of equations in an efficient and stable manner. This section is meant to give a brief general assessment of the state-of-the art from an application viewpoint and summarize the information obtained from the literature survey. A complete description of all the techniques being used is beyond the scope of this report.

The critical issue of numerical schemes for supersonic flow is the accuracy with which shock waves are resolved. Note that inlet applications are not unique in this regard; schemes that work for general supersonic problems will work for inlet applications. The classical numerical methods use finite difference representations of the governing equations. Because the difference equations are derived from Taylor series, their solutions must be continuous. Thus shock waves are represented by steep gradients, rather than true discontinuities. Typical results for older codes using classical first and second order differencing will have dissipative smearing and dispersive oscillations near steep gradients due to the truncation errors of the Taylor series approximations. Artificial dissipation or damping is usually necessary to control the dispersive oscillations for stability. Flux splitting techniques provide directional differencing that represents the natural wave propagation directions of the governing equations. This helps reduce dissipative errors and steepen the shock gradients. Two classical methods have been predominant in the CFD codes applied to inlets according to the literature search. MacCormack's predictor-corrector method in various explicit and implicit formulations has been used for unit problems and complete 3-D inlet calculations. The Beam-Warming implicit method is implemented in the familiar PARC series of codes, and most major airframe contractors have proprietary versions. These codes are routinely used for inlet applications of all types.

The most recent scheme developments are able to blend low order methods near discontinuities with high order methods in smooth regions of the flow.²¹ These developments are based on finite volume formulations of the governing equations. All of the following methods were encountered in the most recent inlet application references: various upwind schemes, Riemann solvers, total variation diminishing (TVD) schemes, and monotone upstream centered schemes (MUSCL). These advanced schemes have proven to be fully capable of accurately predicting the inviscid shock structures of any practical inlet geometry. Scheme development has not been a restrictive technology issue for inlet applications for several years.

Efficiency improvements will always be in demand as CFD is applied more for design. Minimizing the number of iterations (time or pseudo-time integration steps) to converge to a steady-state condition is critical in determining the number of parameters that can be investigated in a design application. Again, inlet applications are not unique in this regard. The latest methods which have been applied are localized time stepping, Newton iteration, Runge-Kutta iteration, and multi-grid techniques.

4.0 BOUNDARY CONDITIONS

Since the Navier-Stokes equations and the subsets are initial-boundary value problems, the boundary conditions define their unique solutions. Although mathematical analysis indicates the number and type of boundary conditions required for various physical boundaries, there is no rigorous theory for *numerical* implementation of boundary conditions. Heuristic analysis is often used to develop and test numerical techniques which exhibit the appropriate physical behavior. Equations with hyperbolic or elliptic characteristics are particularly sensitive to boundary conditions because disturbances and errors are propagated to other regions of the domain.³

Boundary conditions for high speed inlet flows are more complicated than most other applications. Inlet flows have multiple supersonic and subsonic regions in the same domain, solid walls with various thermal constraints, bleed and/or blowing regions, external spillage, etc. Treatment of boundary conditions for inlet applications is extremely important to yield meaningful results. A discussion of boundary condition types encountered in this survey is given below.

4.1 Freestream/Inflow Conditions

This is the easiest condition to apply for high speed inlets and related flows. Since the flow is supersonic, characteristic theory dictates that the freestream boundary should not be affected by other points in the field. Thus it is appropriate to fix the flow variables at the freestream boundary in time and space. The only requirement is that the specified conditions fully define the conservation variable vector U at every point on the boundary. The condition can be specified as total conditions or static conditions or combinations thereof which can be manipulated with the usual gas dynamic relations.

Most applications to actual inlet geometries have uniform freestream conditions. Specification of a freestream Mach number, total pressure, and total temperature are sufficient to define the state of the gas on the entire boundary. Some applications specify upstream boundary flow profiles in order to avoid computing the flow outside the region of interest. Even the subsonic portion of the boundary layer is elliptic, the freestream boundary can be placed far enough upstream that the pressure gradient will not be influenced by events downstream. Then the upstream profile can be held fixed without violating the physics of the problem. For example, shock wave-boundary layer interactions have a limited region of upstream influence. Because the flow ahead of this region is not affected by the interaction, it is not necessary to solve for the developing boundary layer far upstream of the interaction. Specification of the profile has been accomplished by three different methods in this survey: 1) computing a flat plate boundary layer prior to computing the solution on the region of interest, 2) assuming a turbulent profile anchored with limited test information (skin friction, displacement thickness, etc.), or 3) matching a measured pitot pressure profile. References 2, 13, 16, 22, 23, 24, 25, 26, and 27 have all used these techniques successfully for 2-D and 3-D interaction problems.

For turbulent calculations with two-equation turbulence models, the turbulent conservation variables also need to be specified at the inflow boundary. Description of the models and details of the boundary conditions that have been used is given in Section 6.2.

4.2 Wall Boundaries

Solid walls have velocity conditions and heat transfer conditions in viscous flow. The velocity condition is the no-slip condition, i.e. the fluid velocity at the wall is the same as the wall velocity. None of the applications reviewed here had moving walls, so the velocity at the wall is simply set to zero. The heat transfer condition can be adiabatic, a specified heat transfer rate, or a specified temperature. If the heat transfer is specified or adiabatic, then the wall temperature is determined as part of the solution, and vice versa. Numerically there is no difficulty with either condition, and many codes can handle both. A specified wall temperature usually remains fixed in time but can vary spatially. A specified heat transfer rate involves a simple difference approximation to the temperature gradient normal to the wall.

Although the heat transfer boundary conditions are easy to implement numerically, it is challenging to specify conditions that realistically model a particular physical situation. A realistic condition depends upon the heat transfer of the inlet structure which can be non-uniform and time dependent. For test models in high Mach blow-down wind tunnels, a constant cold wall temperature is a good approximation because the model may not heat up appreciably over the short duration of the run. The P8 inlet is a good example here. From Reference 10, the typical run time is only 1-4 minutes and the model leading edges were water cooled. The wall temperature increased from the ambient condition by 15%, at most, over a 20 second time span. Brenneis and Wanie⁹ performed calculations on the P8 with constant temperature and adiabatic wall boundary conditions. The results for the adiabatic case were not in good agreement with the test data and the solution predicted a small separation bubble not observed in the experiment. References 28 and 29 also used constant wall temperature conditions for the P8 based on the reported test data. For continuous flow tunnels or flight conditions, the steady-state wall temperatures and/or heat transfer rates are rarely known in sufficient detail for a full specification of all wall boundaries. From the reference survey, the rule-of-thumb is to use adiabatic conditions for test models in continuous flow tunnels. This is probably a reasonable estimate for uncooled test models since heat conduction away from the model is limited. Also, for geometries which have no associated wind tunnel test or heat transfer analysis, the adiabatic condition has been used most frequently. The adiabatic condition at least yields the upper limit of wall temperature, which might indicate if cooling is needed for a piece of hardware.

Wall pressure determination requires consideration of the wall normal momentum equation. One condition is to set this gradient to zero,

$$\frac{\partial P}{\partial \eta} \Big|_{wall} = 0 \quad , \quad 4.1$$

per the usual thin boundary layer assumption for high Reynolds number flows. This is the most common condition from the survey results and it is easy to implement: the pressure at a wall point is set equal to the pressure at an adjacent point normal to the wall. This is may not be a good approximation for hypersonic flows because the thin boundary layer assumption loses validity.⁴ Large magnitude local wall curvature also tends to produce a non-zero normal pressure gradient.

Alternatively, the steady state normal momentum equation written explicitly for the

pressure gradient is used. Since the wall velocity components are zero (assuming no bleed is present), all convective terms drop out and the normal momentum becomes:

$$\frac{\partial P}{\partial \eta} \big|_{wall} = \text{viscous stress derivatives} \quad 4.2$$

The right-hand side in complete form would contain all the viscous stress terms in Equation 2.3, transformed into a wall aligned coordinate system. Some of the reference applications neglect viscous derivatives in the tangential directions in favor of the normal direction, which results in a reduced normal momentum equation. These simplifications are tending to the limiting case of Equation 4.1. Theoretically, a reduced normal momentum equation should be more accurate than the zero normal pressure gradient assumption since more terms are retained. Shang et al.^{30,31} have used both methods for shock wave-boundary layer interactions and supersonic compressing corner flows with practically identical results. These results were for solid walls with no bleed. When wall transpiration is involved, the form of the wall normal momentum equation becomes more important, as discussed in the next section.

Other methods are also being used for the wall pressure gradient. In the sublayer approximation for the PNS calculations of Kim et al.¹⁶, a centrifugal force balance equation is used:

$$\frac{\partial P}{\partial \eta} \big|_{wall} = \frac{\rho V_t^2}{R} \quad 4.3$$

where V_t is the tangential velocity at the grid point adjacent to the wall and R is the local radius of curvature. Liou et al.¹² use an unsteady characteristics method to determine wall pressure directly in the inviscid operator of their numerical integration scheme.

For Euler solutions, wall boundary conditions require that the velocity vector be tangent to the wall since mass flux can not pass through solid walls. This is more tedious to implement numerically than the zero velocity condition for viscous flows. None of the Euler application references discuss in detail how wall tangency is implemented. Anderson, Tannehill, and Pletcher³ outline two methods in their text book: a reflection procedure which involves mirroring the normal velocity component and thermodynamic variables about the wall boundary to extra grid points beyond the boundary, and Abbot's method which introduces isentropic compression or expansion waves to turn a misaligned velocity vector parallel to the wall.

Accurate specification of wall normal gradients for pressure or temperature can be affected by the grid topology. The normal gradients evaluated as one-sided difference approximations imply that grid lines in the η -direction are normal to the wall everywhere, a subtle detail not often discussed in application references. Grid orthogonality is not required to obtain a solution, but too much deviation from orthogonality will produce unacceptable truncation errors.^{32,33} Thompson³³ indicates that, in general, near orthogonality at the boundaries should be achieved. None of the application references reviewed here investigated the effect of grid orthogonality. Other grid considerations are discussed in Section 5.0.

4.3 Bleed Boundary Conditions

Boundary layer bleed subsystems are used to control shock boundary layer interactions in high speed inlets. Porous wall plates and slots function to remove all or part of the low energy air near the wall by ducting it to a low pressure plenum and discharging it overboard. Bleed location and amount are critical design parameters for control of shock induced separations and overall performance of the inlet. Bleed boundary conditions are therefore an important aspect of computational analysis of realistic inlet systems.

For porous wall bleed, it has been impractical to model the individual bleed ports in a CFD solution. The large number and small scale of the bleed ports would result in prohibitively large grids and CPU time. Instead, a mass flux is determined which is allowed to transpire through the wall at the discreet grid points in the bleed region. The most common approach is to specify a uniform mass flux distribution across the bleed region based on total mass flow rate at the bleed plenum exhaust.³⁴⁻³⁹ This is straightforward for computing solutions on experimental hardware where the total bleed mass flow rate is measured. For design purposes, the constant flux specification is based on a desired amount of boundary layer removal. The amount is specified as a percentage of the mass flow in the boundary layer or a percentage of the total inlet mass flow rate. Trial and error procedures are necessary since details of the boundary layer and inlet flow are not known a priori. Rizetta³⁵ experienced difficulty in obtaining solutions when the wall velocity changes abruptly from zero to the corresponding bleed normal velocity between adjacent grid points. A ramping function has been used to gradually increase the mass flux from zero to the uniform level over a few grid points.^{16,35}

The uniform mass flux bleed boundary is convenient when the only information available is the total bleed mass removed. It does not exhibit the true nature of the flow in the bleed region because the mass flux is generally not uniform, especially when shocks fall across the region. Experimental results indicate that the bleed mass flux increases with wall pressure.²⁵ The plenum beneath the porous plate will have elliptic upstream influence, and strong pressure gradients across the plate can result in reduced bleed flux or even recirculation in the forward parts of the bleed region. Some applications have specified a non-uniform bleed flux distribution based on more detailed experimental information.^{16,40-42} This is an improvement only if the final wall pressure distribution predicted by the CFD solution matches that in the experiment. If the wall pressure is different than the experiment, then the mass flux distribution is not consistent with the experimental conditions.

There are current ongoing efforts to compute the small scale flowfields in isolated bleed ports. The hope is that by understanding the detailed aerodynamics of single ports, more realistic bleed flow models can be developed to improve boundary conditions for inlet calculations on the macroscopic level. Hamed et al.⁴³⁻⁴⁵ have computed an isolated bleed slot on a flat plate with and incident shock wave. Their results (Figure 4-1) show that the flow in the slot acts like a convergent-divergent passage, which becomes choked when the plenum pressure is reduced below a certain value. The velocity distributions show that the normal velocity is loaded towards the trailing edge of the slot opening, behind the incident shock. Also the tangential velocity component is not zero (as is normally assumed) and actually reverses to an upstream direction near the trailing edge.

In all but two of the applications reviewed here, the wall tangential velocity is simply

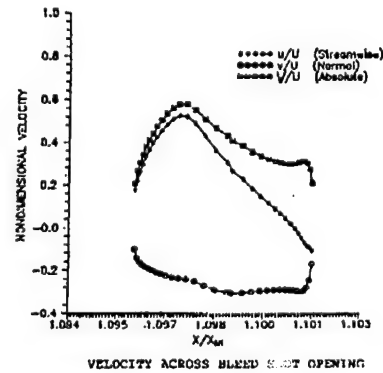
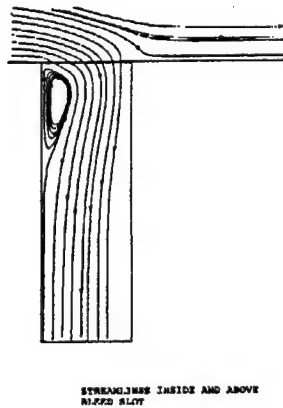
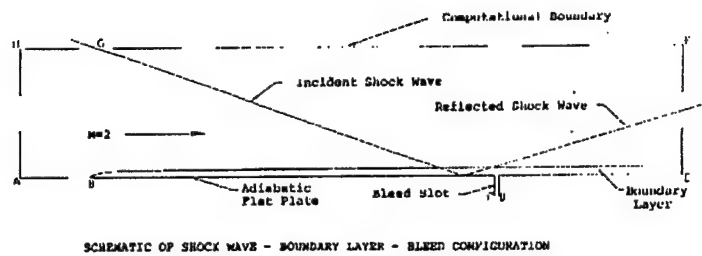
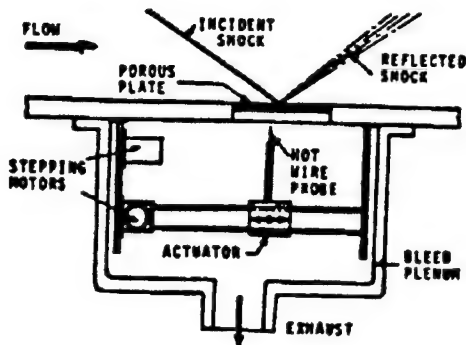
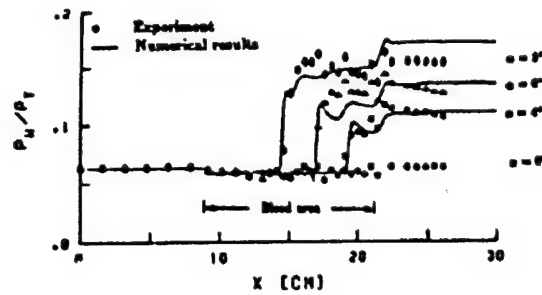


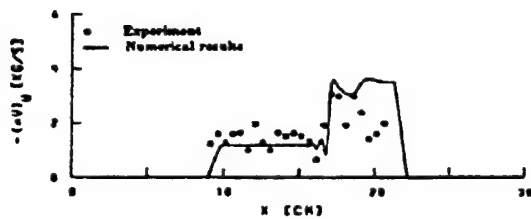
Figure 4-1 Bleed Slot Calculations (Ref. 43)



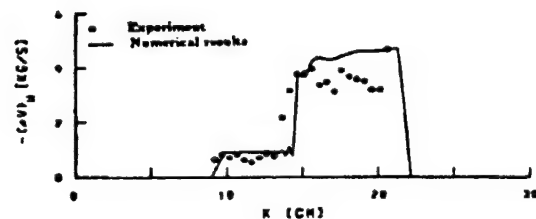
Apparatus for bleed measurement



Wall pressure distributions with suction



Bleed Distribution; $\alpha = 6^\circ$



Bleed Distribution; $\alpha = 8^\circ$

Figure 4-2 Incident Shock-Boundary Layer Interaction with Bleed (Ref. 25)

specified to be zero for lack of additional information. In one exception, Hunter et al⁴¹ have used additional equations assuming constant entropy along streamlines in the bleed region which allows the wall density and tangential velocity to evolve as part of the solution. The normal velocity is still determined from a specified mass flux. Shigematsu et al⁴² have used this same approach for a Mach 3 mixed compression inlet. None of the applications references discuss the impact of the bleed tangential velocity component on the accuracy of results obtained.

Researchers have also been attempting to model porous wall bleed more realistically by coupling the bleed mass flux with the static pressure in a fictitious plenum, without actually computing the plenum flow. The basic method is to use the pressure difference between wall and the plenum to determine the mass flux through the bleed openings. Losses are incurred via empirically derived flow coefficients (discharge, velocity, total pressure loss, etc.) for the bleed ports. Abrahamson and Brower⁴⁶ developed an initial approach by treating the bleed ports analytically as isentropic convergent passages which may be choked or unchoked. The wall tangential velocity is assumed to be zero but the normal velocity is determined from the local wall pressure, a specified plenum pressure, and an empirical velocity coefficient. The velocity coefficient at each grid point was adjusted to match the experimentally measured mass flux distribution in an incident shock-boundary layer interaction test case. The end result is still a specification of a measured mass flux distribution by an indirect method. They admit that this is not a complete verification of the method and that the velocity coefficient will be a function of Mach number, Reynolds number, port geometry, etc. This method does have good potential assuming empirical relations can be developed for the bleed port flow coefficients across a wide range of conditions.

Benhachmi, Greber, and Hingst²⁵ conducted a combined experimental and numerical investigation of a porous flat plate with an incident 2-D shock wave. The porous area was a woven mesh material backed by a honeycomb as opposed to a solid plate with holes. Their experiments included measurements of surface pressure and temperature across the bleed region as well as mass flux distributions entering the plenum. The CFD analysis included an empirical bleed method relating the mass flux distribution to the wall static pressure and a specified plenum pressure. The air resistance to the porous mesh was calibrated prior to the incident shock test conditions to yield an equation of the form:

$$\frac{\Delta P}{\rho V^2} = A + \frac{B}{Re_1} \quad 4.4$$

where Re_1 is the Reynolds number based on the mesh thickness, and A and B are empirical constants. It is assumed though not completely clear that V is the normal wall velocity component resulting from the pressure difference ΔP . The tangential velocity is still taken to be zero in the CFD analysis. Equation 4.4 was used as a boundary condition for cases involving incident shocks created by wedge angles of four, six, and eight degrees. A typical result of the mass flux and wall pressure is shown in Figure 4-2 for the six and eight degree cases. The perturbations in the measured mass flux in the bleed region are due to roughness of the mesh material, small steps in the transition from non-porous to porous walls, and possible resonance in the plenum. The CFD results have smooth oscillations probably due to insufficient streamwise grid resolution according to the authors; these should not be construed as the same perturbations

in the test data created by the mesh roughness. The authors comment that bleed region roughness and pressure waves emanating from the plenum are impractical to model in a discretized numerical analysis. Qualitatively, the calculated bleed flux increases with the wall pressure, which was the desired result of this bleed boundary condition. The predicted bleed mass flows using the calibrated loss coefficients are within seven to twelve percent of the measured flow rates, which the authors suggest is good for engineering applications considering the simplicity of the model.

The bleed boundary conditions are also dependent on the wall pressure gradient assumptions discussed in Section 4.2. This is due to the fact that the streamlines in the boundary layer are turned toward the wall when suction is applied, and streamline curvature cannot occur without a pressure gradient. Thus assuming zero normal pressure gradient is not physically correct for bleed boundaries, even though it is used quite often for simplicity. Abrahamson and Brower⁴⁶ applied both the zero normal pressure gradient condition and the reduced normal momentum equation to their bleed boundary condition, with the latter case yielding a better match to the test data as expected. Rizetta³⁵ mentions that the inclusion of the normal pressure gradient equation resulted in "smoother behavior of the flow variables" than the zero normal pressure gradient assumption. Benhachmi et al.²⁵ also used the reduced normal momentum equation for their bleed boundary condition study.

Large bleed/bypass slots typically found at the throat of external and mixed compression inlets have been modeled directly in two or three dimensions, with the slot opening and plenum chamber as part of the grid geometry. The flowfield near the slot opening involves imbedded shocks, subsonic pockets, and rapid turning into the plenum. The slot flow and the inlet subsonic duct flow are highly coupled, which is critical for inlet stability. It is not likely that a wall grid with a mass efflux boundary condition spanning the slot opening will accurately replicate this complex physical situation. As an example, Fujimoto, Niwa, and Sawada¹⁸ have done a realistic mixed compression inlet calculation including ramp slot bleeds and a throat bypass slot with the plenums and exhaust ports included. Some of their results were shown in Figure 2-11. No test data is available but this is an excellent illustration of the complexity involved in a good design application.

4.4 Supersonic Outflow Boundaries

Supersonic outflow boundaries for inlet applications are those which involve supersonic flow leaving the computational domain. The desired condition is that any waves (shocks, Mach waves, etc.) pass through the boundaries without reflection in accordance with the direction of the flow characteristics at that boundary. This is very beneficial because these boundaries can be placed close to the region of interest without influencing the solution and therefore reduce the domain size. Also, mixed compression inlets which maintain supersonic flow throughout the internal duct (such as the P8) are simulated with a supersonic outflow boundary at the duct exit.

The nonreflective property is accomplished by extrapolating the flow variables at the boundary. The implementation of extrapolation boundary conditions is straightforward by two methods. The first method is to simply specify zero gradients in the conservative variables in a direction normal to the boundary:

$$\left. \begin{array}{l} \frac{\partial U}{\partial \xi} \\ \frac{\partial U}{\partial \eta} \\ \frac{\partial U}{\partial \zeta} \end{array} \right\} = 0, \quad \text{applied on constant} \left\{ \begin{array}{l} \eta - \zeta \text{ boundary} \\ \xi - \zeta \text{ boundary} \\ \xi - \eta \text{ boundary} \end{array} \right. \quad 4.5$$

This is numerically applied with a two or three point backward difference. The application references use different terminology to describe this condition without giving the details, including "nonreflective boundary", "extrapolation boundary", and "zero flux gradient."

The second method is a characteristics based boundary condition. The Riemann invariants for unsteady wave motion,

$$\Delta P + (u \pm a) \Delta \rho = 0 \quad 4.6$$

are used to extrapolate the boundary points along the characteristic directions. This condition is based on the physics of the flow but more complex to implement numerically. The direction of the characteristics and their intercept points on the boundary must be determined and may require an iterative process. Terminology for this condition is "Mach wave extrapolation" or "characteristic boundary."

The zero flux gradient condition has been the most widely used according to the application survey, probably due to its simplicity and satisfactory results. Both methods work well as long as the boundary is a reasonable distance away from high flow gradients in the region of interest. "Reasonable" means the region of interest is not influenced by the boundary, which may require some numerical experimentation.

4.5 Subsonic Outflow Boundaries

A boundary where subsonic internal duct flow exits an inlet configuration needs special consideration. The exit pressure and massflow rate are critical parameters for determining the inlet operating point and performance. Pressure and massflow depend upon the downstream device which is throttling the inlet (an engine for air vehicles, a massflow plug for test hardware, etc.). Actually, the boundary itself is a computational artifice because the throttling device is too complicated to simulate in a CFD solution or the physical situation may not be well defined.

High pressure subsonic exit conditions impose a strong upstream influence on the inlet shock structure which affects boundary layer interactions, massflow control, and inlet stability. To simulate these effects, subsonic exit conditions must propagate information from the boundary to the interior grid points. From 1-D unsteady wave theory, subsonic flow has two positive slope characteristic propagating from the interior towards the boundary and a negative slope characteristic propagating from the boundary towards the interior.^{12,38,39} Thus one flow parameter may be specified on the boundary and the others are extrapolated from the interior.

The most common approach is to specify a uniform static pressure along this boundary.^{17,18,24,47,48} The pressure level determines the inlet operating point and massflow rate in

the steady-state solution. Alternatively, a certain massflow rate (corrected or actual) may be desired at the exit. This is accomplished by integrating the boundary after each iteration to determine the actual massflow rate. Then the pressure level is adjusted as the solution develops to rectify any difference from the desired massflow rate, but the effect is still a uniform exit pressure.

One drawback to the uniform static pressure boundary is that the flow entering an engine or massflow control device is not constrained to have uniform static pressure. This can be a problem if the diffuser flow path has relatively high curvature near the exit. Two methods have been used to avoid this problem. The first is to add a constant area straight section of grid to the diffuser exit and specify the uniform pressure level at the exit of the straight section, as shown in Figure 4-3. The length of the section may be on the order of a few duct diameters or duct heights, which helps remove the uniform exit pressure constraint from the point of interest. The disadvantage is that additional grid points are needed for the solution. The other approach is to add a "computational" nozzle to the diffuser exit. This is a convergent-divergent section added to the diffuser exit which controls massflow rate by the size of the throat. The nozzle exit boundary is an extrapolation condition as discussed in Section 4.4 since the flow is reaccelerated to a supersonic Mach number. This is a realistic simulation because it throttles the inlet in a similar way as an engine exhaust nozzle or massflow plug. However, it can also be computationally expensive. Before a solution is obtained, the nozzle throat area must be sized from estimates of total pressure loss through the inlet and an estimated nozzle discharge coefficient. Any fine tuning of the throat area to get a desired massflow rate requires both a new nozzle grid and a restart of the solution. Shigematsu et al.⁴² obtained 2-D solutions of a mixed compression inlet with various nozzle exit-to-throat area ratios as shown in Figure 4-4. In this case the "computational" nozzle is handled by their flow solver such that only the throat area needs to be specified; the nozzle grid is automatically regenerated internally by the code. The decreasing nozzle throat area results in enlarged separated regions in the diffuser as the increased back pressure feeds forward. Experience suggests that similar events would occur in a wind tunnel test.

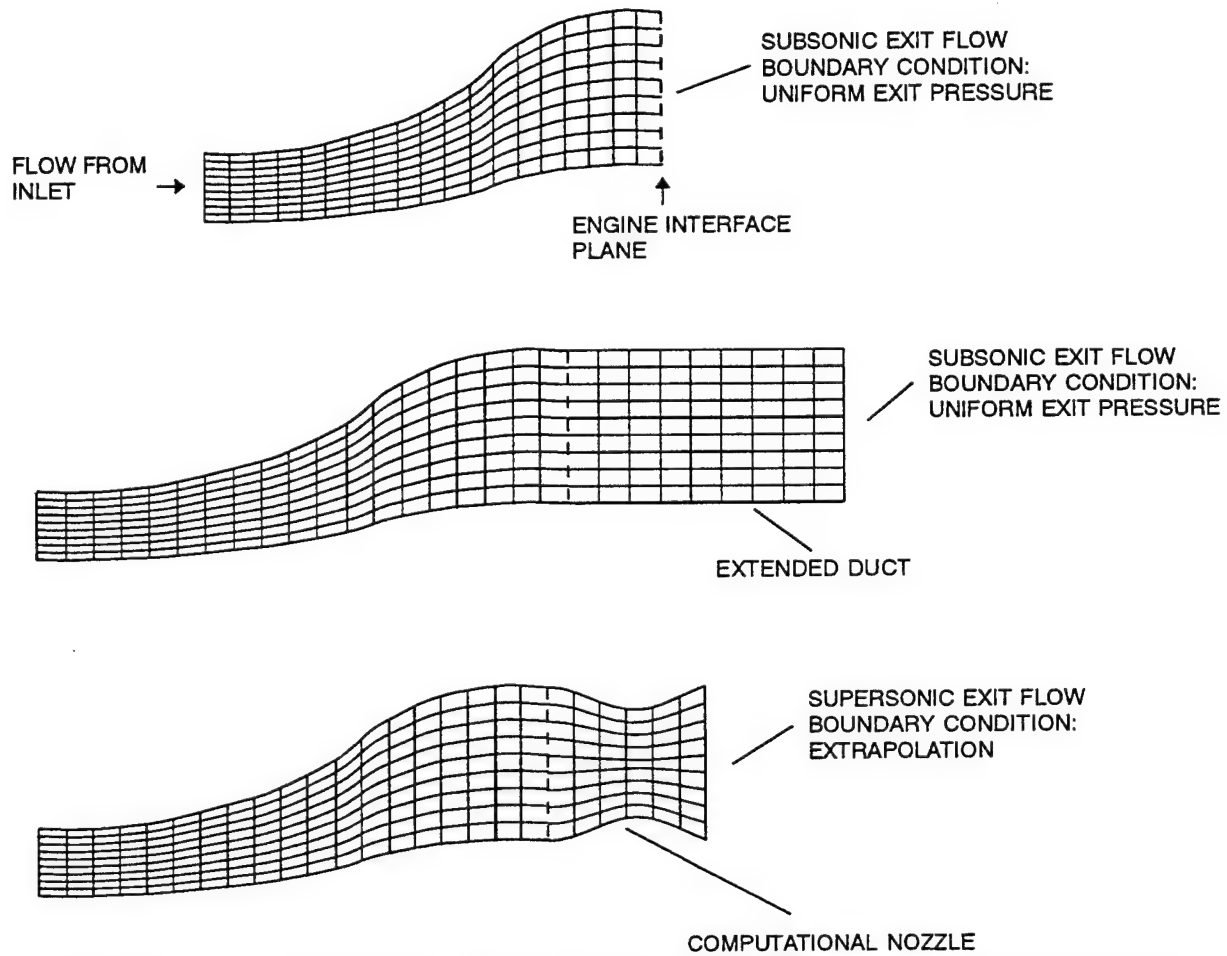


Figure 4-3 Gridding Techniques for Diffuser Exit Boundaries

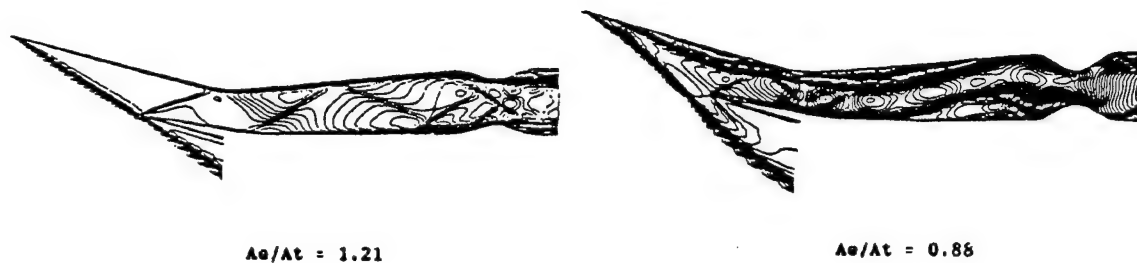


Figure 4-4 Mixed Compression Inlet with Computational Nozzle Exit Boundary (Ref. 42)

5.0 GRID REQUIREMENTS

Grid generation appears to rely heavily upon personal experience with CFD applications. There are few guidelines when starting a new application. Often some adjustments are made after an initial solution is obtained to improve the grid quality in certain regions. Complexity of the grids for applications reviewed here range from simple single block rectangular geometry for shock wave-boundary layer interactions to complex multiblock arrangements for complete inlet hardware.

The importance of grid orthogonality at the boundaries has already been discussed in Section 4.2. Also, smooth variation of the grid spacing is desirable to integrate efficiently to a converged steady-state solution.³² Abrupt changes in grid spacing leads to large truncation errors and possible departure. Closely spaced grid points are desirable in regions with high gradients, e.g. shocks and boundary layers, to reduce numerical truncation errors. However, computer memory limitations and processor requirements can restrict the total number of grid points. Thus the CFD applier must trade accuracy against computer costs when generating grids. More often than not, geometric simplifications are made to reduce grid complexity as much as possible.

A common example of geometric simplification is the assumption of perfectly sharp ramp and cowl leading edges. The assumption of a sharp leading edge greatly simplifies the gridding task and eliminates an otherwise densely packed grid around a blunt leading edge. The P8 inlet had a cowl lip radius of 0.045 inch, which definitely displaced the cowl shock forward of the lip highlight station. Knight²⁹ simulated this displacement with a sharp cowl lip 1.1 inches forward of the actual lip highlight such that the cowl shock would strike the ramp shoulder at the right location (Figure 5-1). However, the entropy layer created by the blunt lip is ignored by this technique.

5.1 Shock Wave Resolution

State-of-the-art integration schemes are currently capable of capturing shocks with three to four grid points. The most recent scheme development has been focused on capturing shocks without producing dispersive errors (post shock oscillations). However, many "production" codes being applied to inlets still can produce significant post shock oscillations because they are based on less advanced integration schemes. If the grid spacing happens to be large where a shock is located, then the shock will be smeared over a non-physically large distance, which might affect critical shock boundary layer interactions. Successful CFD appliers make an estimate of shock locations and construct the grid accordingly to yield crisp shock capturing with minimal overshoot. Also, adaptive grid techniques have been used to pack the grid near shocks as the solution develops to a final steady-state.

5.2 Boundary Layer Resolution

Turbulent boundary layer resolution also demands high grid density near solid walls. The parameters used to describe the grid spacing at the wall are closely related to turbulent boundary layer theory and the dimensionless inner variables:

$$y^+ = \frac{y v_w^+}{\nu_w} \quad u^+ = \frac{\bar{u}}{v^+} \quad v^+ = \sqrt{\frac{\tau_w}{\rho_w}} \quad 5.1$$

where ν_w , τ_w , and ρ_w are the kinematic viscosity, shear stress, and density at the wall, respectively. A typical incompressible turbulent boundary layer profile in these coordinates is shown in Figure 5-2 with the different regions identified. The location of the first grid point from the wall is important to get accurate wall shear stress and heat transfer. This location is measured in terms of the wall normal coordinate y^+ . Since y^+ depends upon the local wall shear stress, the applier will not know the exact value for the first grid point prior to obtaining the solution. Estimates from flat plate profiles are used to construct the initial grid, with adjustments made as the solution progresses. The final quality of the grid is often reported in terms of all the grid points next to solid walls being less than a certain y^+ threshold. A satisfactory value for y^+ is a matter of debate, and depends upon the assumptions of the turbulence model being used (Section 6.0). Wall shear stress and heat transfer accuracy improves with closer spacing. Also, it is generally known that accurate heat transfer prediction demands closer spacing than accurate shear stress prediction. But extremely small spacing can severely restrict the allowable integration time step for stability which results in excessive iterations to convergence.

From the reference applications, values were reported from $y^+=.07$ to as much as $y^+=8$, with most reported values in the range $y^+=1-5$. A general observation from the references reviewed here and discussions at technical conferences and symposia is that $y^+=1$ is considered to be quite good. The perception is that the applier did not sacrifice boundary layer resolution in order to get an economic solution. Agarwal^{6,49} and co-authors suggest that y^+ should be at most one for accuracy in skin friction calculations. This conclusion is supported by numerical experiments which showed that skin friction becomes independent of normal grid spacing when y^+ is less than one.

Some turbulence models require use of a wall function.^{24,28,50} The wall function is an analytical expression for the turbulent boundary layer profile between the wall and the first grid point from the wall. A typical expression is the familiar logarithmic law-of-the-wall:

$$u^+ = \frac{1}{\kappa} \ln y^+ + B, \quad \kappa \approx .41, \quad B \approx 5 \quad 5.2$$

To use a wall function, the solution is integrated on the interior points as usual, but boundary conditions are applied at the first point off the wall rather than at the wall. These boundary conditions are related to the wall shear stress via the wall function. The first point off the wall should be located in the logarithmic region, such that much larger values for y^+ can be used with corresponding increases in stable time integration step sizes. For the applications referenced (24,28,50), wall normal grid spacing up to $y^+=30$ was used. Using a wall function assumes that the logarithmic near wall profile exists throughout the flow. This is not likely for inlet flows with strong shock wave-boundary layer interactions, and therefore the wall functions have not seen much application in this area.

The number of grid points in the turbulent boundary layer is also reported in application references as a measure of refinement at solid walls. These values ranged from 10 to 40 points

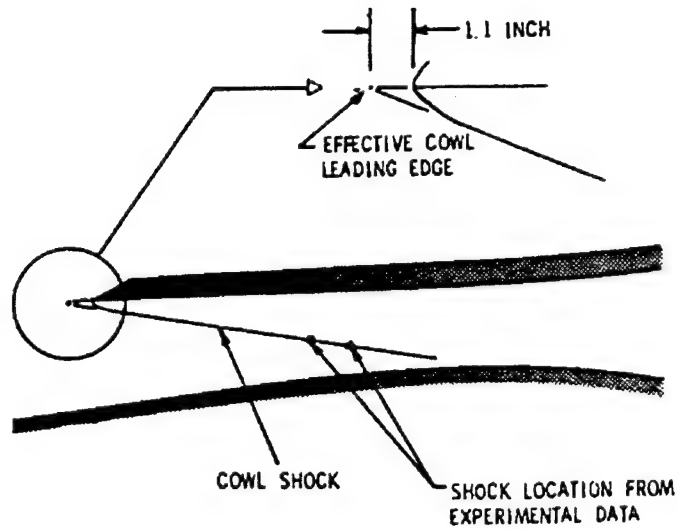


Figure 5-1 Sharp Lip Extension on the P8 for Grid Simplification (Knight, Ref. 29)

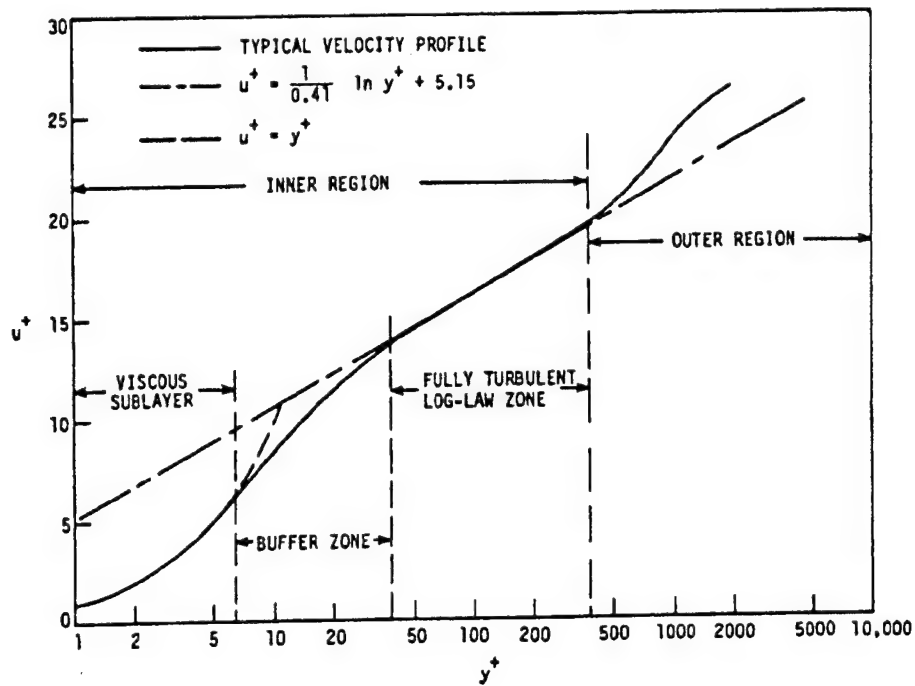


Figure 5-2 Turbulent Boundary Layer Nomenclature (Ref. 3)

in the boundary layer, tending toward the higher numbers. Furthermore, the number of points in the viscous sub-layer was also reported in the range from 2 to 18. Again, the applier will not know beforehand the actual boundary layer thickness, so estimates must be used initially.

Some appliers carefully investigate the effect of grid point density on the simple unit problems before attempting a more complicated configuration. Such problems are small enough that several solutions can be obtained to optimize the grid spacing. It is generally true from the application references that grid refinement in the boundary layer is diminished as larger and more complicated configurations are attempted. This is evidence that computer economics is a strong driver in grid generation.

6.0 TURBULENCE MODELS AND TRANSITIONS SIMULATIONS

High speed inlet flows of interest are mostly turbulent. The Boussinesq assumption discussed in Section 2.2 introduces the proportionality coefficient, μ_p , but does not offer any information about its numerical value. The eddy viscosity coefficient is not a property of the fluid like molecular viscosity. Rather, it is a property of the flowfield and depends upon the flow conditions and geometry.⁵ Turbulence models attempt to simulate this dependency through analytical, empirical, and heuristic reasoning. The most common models encountered in this review, their modifications, and successfulness of the applications are discussed below.

6.1 Zero-Equation Models

The zero-equation models are referred to as algebraic models. None of the parameters in the model are additional dependent variables to be solved with Equations 2.1-2.4. They are merely evaluated with algebraic closure expressions that depend on the local flow conditions. They are relatively fast and require a negligible amount of additional computer operations. However, they are also strongly empirical and therefore not universally applicable without modifications for specific types of flows. It will be shown that the existing algebraic models have serious deficiencies for high speed inlet applications. However, they will continue to be employed because of their relative simplicity and widespread incorporation into existing Navier-Stokes solvers.

The Cebeci-Smith and the Baldwin-Lomax models have been the primary algebraic models used in high speed inlet applications. They are both two-layer models with different formulations for the inner and outer regions of the boundary layer:

$$\mu_t = \begin{cases} \mu_{t,inner}, & y \leq y_c \\ \mu_{t,outer}, & y > y_c \end{cases} \quad 6.1$$

where y_c is the "crossover" point separating the implementation of the two formulations. The outer formulation is used down to the "crossover" point y_c , where it first predicts a lower eddy viscosity than the inner formulation. Then the inner formulation is invoked.

For both models, the inner formulation is based on Prandtl's mixing length theory⁵:

$$\mu_{t,inner} \approx \rho l^2 \left| \frac{\partial u}{\partial y} \right| \quad 6.2$$

where l is the mixing length, represented empirically by

$$l = \kappa y D \quad (\kappa = 0.41) \quad 6.3$$

and D is the Van Driest damping factor:

$$D = 1 - e^{-\frac{y^+}{A^+}} \quad (A^+ \approx 26) \quad 6.4$$

The damping is needed to reduce the eddy viscosity in the viscous sublayer where molecular viscosity dominates. The derivative term in Equation 6.2 is the magnitude of vorticity in a 2-D boundary layer, which is often replaced by the complete vorticity expression in 3-D problems:

$$\begin{aligned} \omega &\approx \left| \frac{\partial u}{\partial y} \right|, \quad 2\text{-D boundary layer} \\ \omega &= \left| \left(\frac{\partial u}{\partial y} - \frac{\partial v}{\partial x} \right), \left(\frac{\partial u}{\partial z} - \frac{\partial w}{\partial x} \right), \left(\frac{\partial v}{\partial z} - \frac{\partial w}{\partial y} \right) \right|, \quad 3\text{-D flows} \end{aligned} \quad 6.5$$

Up to this point, the Cebeci-Smith model and the Baldwin-Lomax model are identical. They differ in the formulation for the outer region. For the Cebeci-Smith model, Clauser's formula for jets and wakes is used^{2,5,25}:

$$\mu_{t,outer} = 0.0168 \rho u_{max} \delta^+ F_{Kleb} \quad 6.6$$

where u_{max} is the boundary layer edge velocity,

$$\delta^+ = \int_0^{\infty} \left(1 - \frac{u}{u_{max}} \right) dy \quad 6.7$$

is the kinematic displacement thickness, and

$$F_{Kleb} = \frac{1}{1 + 5.5 \left(\frac{Y}{\delta^+} \right)^6} \quad 6.8$$

is the Klebanoff correction for turbulent boundary layer edge intermittency. The drawback with this formulation is that the outer length scale depends upon the boundary layer thickness and edge velocity which are not known a priori and might be difficult to determine for shock wave-boundary layer interactions.²³ To eliminate this problem, the Baldwin-Lomax model^{5,23} replaces Clauser's wake model with

$$\mu_{t,outer} = 0.0168 \rho C_{cp} y_{max} F_{max} F_{Kleb} \quad 6.9$$

where $F_{max} = \max \left[y \left| \frac{\partial \bar{u}}{\partial y} \right| D \right]$ and y_{max} is the value of y at F_{max} . The Van Driest damping factor is from Equation 6.4 and the Klebanoff intermittency correction is now

$$F_{Kleb} = \frac{1}{1 + 5.5 (C_{Kleb} y / y_{max})^6}$$

6.10

The Cebeci-Smith model and the Baldwin-Lomax model will produce similar results for flat plate incompressible boundary layers when $C_{cp}=1.6$ and $C_{Kleb}=0.3$.

Note that the above developments and empirical constants are based on incompressible turbulent boundary layers in the absence of strong pressure gradients or wall transpiration. Algebraic models have difficulty predicting separation and reattachment induced by adverse pressure gradients because they are equilibrium models. This assumes that the rates of turbulent energy production and dissipation are equal throughout the flowfield. In their unmodified form, they cannot simulate lag or "history" effects through shock wave-boundary layer interactions.² For compressible turbulent interactions with bleed, blowing, etc., modifications and "tuning" are necessary to get reasonable results. These modifications are discussed below.

A number of modifications for compressibility and wall suction were encountered which involved adjustments to the von Karman constant κ and the van Driest damping thickness A^+ . Rizetta³⁵ simply changed these constants to new values based on 2-D numerical experiments of his Mach 5 inlet application. More complicated expressions for A^+ were used by Horstman et al²⁶ and Abrahamson and Brower⁴⁶ to allow variation with streamwise pressure gradient and wall suction velocity. Both applications were of shock wave-boundary layer interactions. Both papers concluded that A^+ had no impact on the performance of the Baldwin-Lomax for predicting reattachment location. This was attributed to the limited influence of the van Driest damping factor in the outer layer, where y^+ is orders of magnitude greater than A^+ . Visbal and Knight²³ studied the Baldwin-Lomax model for a Mach 2.9 compression ramp shock-boundary layer interaction. They indicated that C_{cp} and C_{Kleb} in the outer layer formulation were functions of the freestream Mach number ($C_{cp}=2.08$ and $C_{Kleb}=0.65$ were required to match compressible Mach 3 flat plate turbulent profiles). A number of researchers have adopted their suggestions or investigated new expressions to allow C_{cp} to vary with edge Mach number in order to improve wall pressure and skin friction predictions for strong interactions.^{22,51,52}

Visbal and Knight also identified a fundamental flaw in the Baldwin-Lomax model when applied to separated interactions. In a non-separated equilibrium turbulent boundary layer, the F function exhibits a single distinct maximum. For separated regions, however, two peaks appear. As the flow reattaches, the inner peak becomes dominant (Figure 6-1). This is indicative of the incoming turbulence equilibrium level being disrupted by the sudden pressure gradient and then relaxing to a new equilibrium state. The multiple peak profile in the separated region makes F_{max} ambiguous. y_{max} can differ by an order of magnitude between the two peaks; selecting the peak closest to the wall yields a non-physical drop in outer eddy viscosity. Visbal and Knight corrected this situation by ensuring that the outermost peak is always selected for F_{max} . However, as the innermost peak in the F function becomes dominant during reattachment, it remains close to the wall such that the eddy viscosity becomes non-physically low again. Sakowski et al⁵¹ addressed this problem by fixing y_{max} upstream of the interaction and determined F_{max} at this constant location throughout the interaction. Another problem was identified by Visbal and Knight in the evaluation of the van Driest damping factor. Since D depends upon wall shear stress through y^+ , the damping factor will become very small when wall shear goes to zero at the

points of separation and reattachment. This causes another non-physical drop in outer eddy viscosity. To alleviate this problem, the wall shear stress is replaced by the local shear stress at points off the wall in evaluating D . This correction has also been adopted by various researchers.^{22,51,52}

An equilibrium relaxation correction to algebraic models was investigated by Shang et al.^{2,30} and Horstman et al.²⁶ for shock wave-boundary layer interactions. This correction attempts to add a history to the turbulence level. Experimental evidence suggests that Reynolds stress is convected along streamlines at constant levels through a sudden adverse pressure gradient, and then exponentially approaches a new equilibrium state.² This was modeled by the following expression:

$$\mu_t = \mu_{t,up} + (\mu_{t,down} - \mu_{t,up}) [1 - e^{-\frac{\Delta x}{\lambda}}] \quad 6.11$$

where $\mu_{t,up}$ is the value of eddy viscosity upstream of the interaction, $\mu_{t,down}$ is the value of eddy viscosity downstream of the interaction, λ is the relaxation length scale, and Δx is the distance from the upstream location. This correction provides remarkable improvement in the prediction of the extent of upstream influence and the overall interaction length for shock wave-boundary layer interactions. The value of λ is probably a function of upstream Mach number and shock strength, ranging from one to twenty boundary layer thicknesses in the references discussed here. A major drawback of this correction is that the position of the interaction must be known beforehand, which limits its usefulness for inlet design applications.

One area where the algebraic models consistently fail regardless of corrections is the reattachment and recovery of separated regions. The skin friction is consistently predicted incorrectly. Ong and Knight²² and Visbal and Knight²³ attribute these failures to a) inability of current CFD techniques to simulate post-shock turbulent fluctuation amplification and natural shock unsteadiness, and b) inability of the algebraic models to simulate dual length scales in a reattaching flow (one for the outer wake, another for the newly developing boundary layer). Based on these conclusions, one cannot expect the algebraic models discussed here to provide accurate flowfield results for a complex high speed inlet. The algebraic models have difficulty with the reattachment region, and shock wave-boundary layer interaction characteristics depend upon the condition of the approaching boundary layer. Thus, mixed compression inlets with multiple shock interactions become progressively corrupted as the solution moves downstream. This is evident in the results of P8 solutions and Rizzetta's³⁵ Mach 5 inlet solution. Still, inlet designers continue to accept the limitations of the algebraic models because of the economical routine application they afford.

There is an interesting aspect to the application of the algebraic models for inlets. The eddy viscosity depends upon the distance from the wall. But inlets may have more than one wall in close proximity to the point of interest. Internal passages have corners and opposing walls with interacting turbulent wake regions. It is possible that the dominating wake region for a given point in a field may not be due to the closest wall. A number of different approaches have been taken to account for the influences of multiple walls on the eddy viscosity at a point in the field. The simplest approach was to simply let "y" be the distance to the closest wall and ignore the influence of other walls.^{16,39,49}

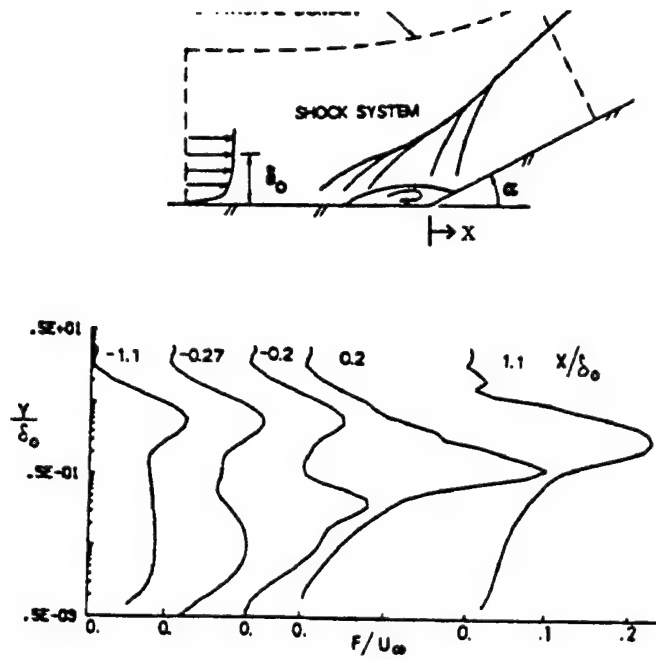


Figure 6-1 Baldwin-Lomax Model F Function Peaks in a Separated Region (Ref. 23)

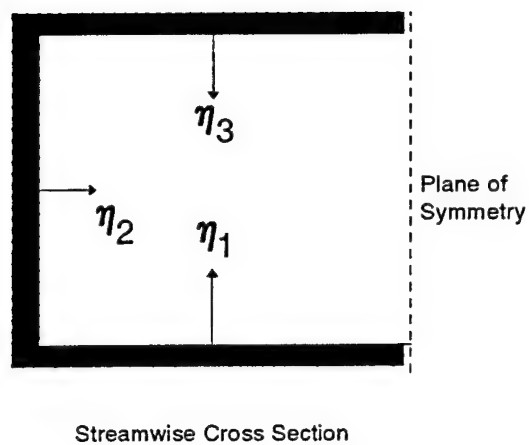


Figure 6-2 Wall Normal Distances for Turbulence Model Applications in Multi-wall Configurations

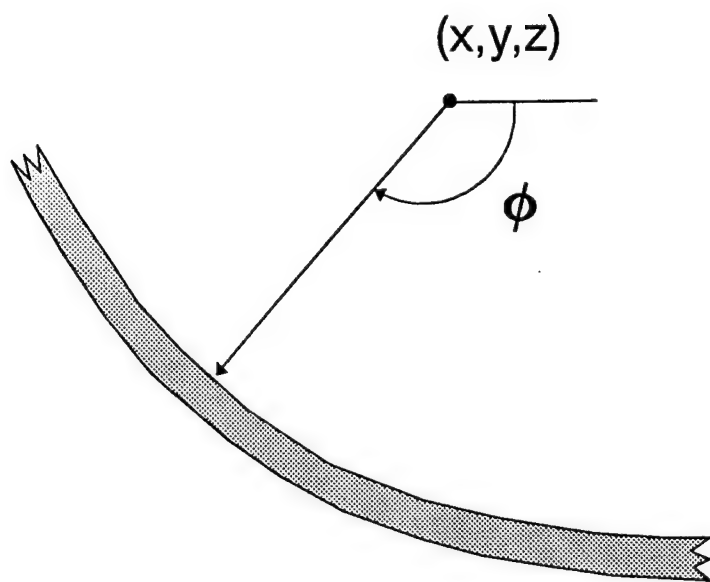


Figure 6-3 Buleev Length Scale, Equation 6.14

Other approaches involve weighting functions based on distance to all walls. Rizetta³⁵ used the following formula for eddy viscosity at a point in the symmetric rectangular duct of the Mach 5 inlet:

$$\mu_t = \frac{\mu_{t_1}/\eta_1 + \mu_{t_2}/\eta_2 + \mu_{t_3}/\eta_3}{1/\eta_1 + 1/\eta_2 + 1/\eta_3} \quad 6.12$$

The enumerated eddy viscosity coefficients are obtained independently for each wall, and η_1 , η_2 , and η_3 are the normal distances to each wall, Figure 6-2. Rizetta admits that there is no physical basis for this formula, but it gives the correct form away from the corners and is continuous. A variation on this formula is given by Ramakrishnan and Goldberg²⁷:

$$\mu_t = \frac{\sum_{i=1}^n \mu_{t_i}/y_i}{\left(\sum_{i=1}^n 1/y_i^2\right)^{\frac{1}{2}}} \quad 6.13$$

This formula places more weight on the closest wall, but again there was no physical basis for this discussed in the reference. Knight^{36,40,53} and Shang et al³¹ have used a more general integral form due to Buleev:

$$l = \left\{ \frac{1}{2} \int_0^{2\pi} \frac{d\phi}{s} \right\}^{-1} \quad 6.14$$

where s is the distance from the point of interest to a point on the wall boundary defined by the angle ϕ (Figure 6-3). This integral results in algebraic expressions for orthogonal corners and rectangular ducts. The length l is then used in the algebraic eddy viscosity model in place of "y". The Buleev length scale is apparently based upon theory and experimental observation of turbulent corner flows.

Still another method was used by Ng et al.⁵⁴ for a 2-D analysis of the P8 inlet. In this situation the lower wall will have a much thicker wake region than the upper wall, and thus the lower wall could have more influence on the eddy viscosity at points which are physically closer to the upper wall. Their method is a two step process which first determines two independent values of eddy viscosity at a point for both the upper and lower walls. Then these values are compared and the greater value is selected to advance the solution.

6.2 Two-Equation Models

The two-equation models are more complex than the algebraic models, but they still invoke the Boussinesq assumption and relate turbulent Reynolds stresses to the flow gradients via the eddy viscosity coefficient. The complexity arises from a functional relationship between the eddy viscosity and two additional dependent conservation variables that describe the velocity and length scales of the turbulence. The two additional dependent variables have their own transport differential equations with terms for convection, diffusion, dissipation, and production. In this way the eddy viscosity is related to the flowfield gradients with minimal empirical presumptions about the shape of the boundary layer profiles.²⁸ The major advantage advertised for the two-equation models is their ability to include upstream influence, or the so-called "history" of turbulent stresses.^{3,11,55} Recall that the failure of the algebraic models for shock wave-boundary layer interactions was attributed in part to the assumption that the turbulence was in equilibrium. The two-equation models do not make this assumption: production and dissipation rates of turbulent energy may be unequal. Therefore one might expect the two-equation models to perform better for such interactions.

Most of the relevant applications of two-equation models to high speed inlet flows were shock wave-boundary layer interaction unit problems. The only application found for an actual inlet with test data was the P8 inlet. This attests to the difficulties of applying the two-equation models in a full Navier-Stokes analysis of a complete inlet geometry. The two additional differential equations add considerable computer memory and processing requirements to state-of-the-art implicit flow solvers. With the need for very fine grid resolution near solid walls, most complete inlet analysis problems quickly exceed available computer resources. Also, the turbulence transport equations are usually very "stiff" (i.e., their solution relaxes slowly from initial conditions to a time asymptotic solution), which requires a large number of iterations to arrive at a converged steady-state solution.

One method of reducing the required computer resources (memory and operations) is to decouple the two turbulence transport equations from the Navier-Stokes equations by time lagging. For each global iteration in time, Equations 2.1-2.4 are first solved with values for the two turbulence conservation variables (and thus μ_t) from the previous iteration. Then, the two turbulence transport equations are solved by themselves using the results of the first step to update the turbulence conservation variables for the next global iteration.

The two-equation models encountered in the literature search involve the turbulent conservation variables k , ϵ , and ω . These variables generally refer to turbulent kinetic energy, turbulent dissipation rate, and specific turbulent dissipation rate, respectively. Relationships between them and the turbulent length scale l are as follows:^{3,24,55}

$$\epsilon \propto \frac{k^{3/2}}{l}, \quad \omega \propto \frac{\epsilon}{k} \quad 6.15$$

The eddy viscosity is found from the turbulent conservation variables via the following relations:

$$\mu_t \propto \rho \frac{k^2}{\epsilon} \propto \rho \frac{k}{\omega} \quad 6.16$$

General forms for the turbulent transport equations are:

$$\left. \begin{array}{l} \frac{\partial}{\partial t} (\rho k) \\ \frac{\partial}{\partial t} (\rho \epsilon) \\ \frac{\partial}{\partial t} (\rho \omega) \end{array} \right\} = \text{convection} + \text{diffusion} + \text{production} + \text{dissipation} \quad 6.17$$

The terms for diffusion, production, and dissipation involve various combinations of flow gradients and algebraic constants which are specific to each model. The combination of the k transport equation with either of the others yields the full two-equation model description.

A particular model is usually associated with the name(s) of its originator. The following table lists the models which were encountered in the literature search:

Two-Equation Models Encountered
in the Literature Search

Name	Type	Notes
Chien	k- ϵ	low Reynolds number
Jones-Launder	k- ϵ	low Reynolds number
Speziale	k- ϵ	low Reynolds number
Launder-Spaulding	k- ϵ	high Reynolds number
Wilcox-Rubesin	k- ω	

In the low Reynolds number form, the two transport equations can be integrated right down to the wall, with y^+ for the first grid point adjacent to the wall on the order of one.^{6,12,28,47,56} High Reynolds number formulations do not model effects near the wall adequately and require the use of a wall function.^{6,24,28} Typical y^+ values for the first grid point are on the order of thirty. Each model has different assumptions and parameters to derive the terms in the transport equations. Little detail is provided in the application references about these terms, and the authors refer the reader to other references for more information. Other modifications have been included for compressibility,^{28,56} thin layer approximation,⁶ and damping of the resultant eddy viscosity in the viscous sublayer where molecular viscosity dominates.²⁴ Some of the references mention that the two-equation models are prone to numerical instabilities, and parameters were added to control them.^{24,28,56}

Additional boundary conditions are needed since two new equations have been added to the system. At the wall, the turbulent kinetic energy is assumed to be zero, and a zero normal gradient is assumed for the dissipation variable. This is consistent with the laminar sublayer next to the wall in which the turbulence is damped out. At an exit boundary, both variables are extrapolated from the interior. At an entrance boundary, the variables are held fixed. Agarwal, Deese, and Peters⁶ used empirical prescriptions for a shock-boundary layer interaction unit problem. The velocity scale is related to freestream Mach number, and the length scale is related to entrance boundary layer thickness. Lowrie⁵⁶ used similar empirical prescriptions for a compression ramp problem, but cautioned that the solution results were sensitive to freestream length scale. Lowrie further suggests that it is appropriate to study the affect of freestream length scale for new applications.

Many of the applications of two-equation turbulence models were directed toward study of model performance and comparison to other models. The collective results of these studies are not conclusive about the superiority of one model over another or two-equation models over algebraic models. Some examples are cited below.

Agarwal, Deese, and Peters⁶ compared several turbulence models for various shock-boundary layer interactions, including separated and non-separated cases. The $k-\epsilon$ model was compared to the Baldwin-Lomax model for a separated normal shock interaction at Mach 1.4. The wall pressure distributions predicted by these two models were identical. Discrepancies to the test data show that the upstream influence is too slight, and the downstream pressure rise is too strong. Both models predict the experimental separation and reattachment points well for this case. The skin friction distribution is improved by the $k-\epsilon$ model downstream of reattachment, however.

Carrol and Dutton²⁴ studied the differences between the Wilcox-Rubesin model with a wall function and the Baldwin-Lomax model for a 2-D normal shock train at Mach 1.61. The two-equation model was superior to the algebraic model, but still not totally in agreement with the test data. The authors indicate that the predicted shock train for both models had a tendency to move farther downstream in the channel than the test shows. The authors arbitrarily raised the channel exit pressure to position the initial shock at the experimentally observed location. The authors suggest that boundary layer growth on the end walls of the test channel (aspect ratio of 2.4) contributed total pressure losses which resulted in a lower exit pressure in the test. The authors also indicate that although the basic flow structure was not affected by grid density, shock train position was dependent on grid refinement in the transverse direction.

Kapoor, Anderson, and Shaw²⁸ applied several algebraic models and all the $k-\epsilon$ models listed in Table 1 except Jones-Launder, to the P8 inlet. The calculations were fully turbulent; boundary layer transition was not simulated. The two low Reynolds number formulations (Chien, Speziale) matched the experimental wall pressures through the cowl shock interaction region quite well. One of the algebraic models was also shown to provide good wall pressure distributions. The high Reynolds number formulation (Launder-Spaulding) over predicted the peak pressure rise produced by the interaction. All the models exhibited too much upstream influence ahead of the cowl shock interaction. The authors attribute this to the fact that the calculations were fully turbulent. This yields a thicker boundary layer than the experimental conditions with transition, which would tend to move the interaction region upstream.

With regards to pitot pressure profiles at the various stations in the P8, the k- ϵ models are generally closer to the experimentally observed boundary layer profiles than the algebraic models. The authors concluded that it is acceptable to use an algebraic model to predict wall pressures for inlets with weak interactions, like the P8, while low Reynolds number k- ϵ models are favored to resolve boundary layer details. However, the review of the Baldwin-Lomax model in Section 6.1 indicates that this is not generally true for strong interactions.

Lowrie extended the low Reynolds number Jones-Launder model to a multi-zone grid approach which is often used for complex configurations to simplify grid generation. The turbulence model and grid zone coupling strategy were tested against a 24° compression ramp unit problem at Mach 2.85, which produces a separated interaction. The k- ϵ model did not accurately predict the extent of the separated region, regardless of whether a multi-zone grid was used or not. The author attributes this failure to the isotropic assumption of the eddy viscosity concept without additional analysis or discussion.

6.3 Boundary Layer Transition Models

It was mentioned earlier that inlet flows are primarily turbulent. There are situations, however, where boundary layer transition occurs and has an affect on inlet performance and more importantly inlet surface heat transfer. This situation is common in wind tunnel tests where the Reynolds number is low compared to typical flight values. This was the case for the P8 inlet, where it was experimentally observed that transition occurred at about 40% of the length of the ramp. It is obviously important to consider transition when comparing, validating, verifying, etc., CFD methods against test data.

Methods encountered for simulating transition in the inlet applications are fairly crude empirical approximations based on flat plate boundary layer experiments. Most of the methods require a specified location of transition onset and/or distance of the transition zone. This is an extremely limiting requirement, because transition details are seldom known or cannot be predicted with current analysis tools for complex 3-D configurations.

A method originally developed by Dhawan and Narasimha in 1958 was outlined by Shang, Hankey, and Petty³¹ and implemented on a supersonic compressing corner at Mach 3. A transition weighting function is given by

$$\Gamma(\bar{x}) = 1 - \exp(-.412\bar{x}^2) \quad 6.18$$

where

$$\bar{x} = \frac{(x - x_{start})}{\Lambda}, \quad x_{start} \leq x \leq x_{end}, \quad \Lambda \approx 2x_{start} \quad 6.19$$

The beginning and end of the transition region are specified by x_{start} and x_{end} , respectively. Λ is a measure of the extent of the region: experimental evidence suggests that the Reynolds number at the end of transition is about twice that at the start. Further details of the implementation were not disclosed, but it is surmised that the weighting function Γ determines the fraction of eddy

viscosity that is actually added into the governing equations:

$$\mu_{total} = \mu_{lam} + \Gamma \mu_{model} \quad 6.20$$

In this implementation, the eddy viscosity from the turbulence model, μ_{model} , must be determined throughout the flow domain. However, only a fraction is added to the laminar molecular viscosity per the exponentially growing function Γ . Note that this method does not actually predict the onset of transition; it only describes how the viscosity varies through the transition region. Shang et al, did not study the performance of this model for their compressing corner problem.

The method of Dhawan and Narasimha was also used by Knight to calculate the P8 inlet in 1977.²⁹ As mentioned above, the transition location of this inlet was experimentally observed. The detailed affects of the transition model were not specifically addressed, but the general results in terms of wall and pitot pressure comparisons are among the best of any applications of the P8 uncovered in the literature search. This is interesting because Knight used the Cebeci-Smith algebraic turbulence model. Other applications of the P8 with fully turbulent flow using algebraic models produced cowl shock induced separation bubbles which were not observed in the test. This suggests that the turbulence models are not completely at fault, and that the condition of the boundary layer approaching a shock-boundary layer interaction must also be simulated correctly.

Another model of transition was used on the P8 by Yaghmaee and Roberts.¹⁴ In this case, the model is capable of predicting the location of transition onset based on local conditions:

$$\frac{Re_{\theta}}{M_e} = constant \quad 6.20$$

where Re_{θ} and M_e are the local boundary layer momentum thickness Reynolds number and edge Mach number, respectively. The constant is an empirically determined threshold. When the ratio on the left exceeds the threshold, the turbulent eddy viscosity is ramped up linearly. Another constant is specified to signal the end of transition, at which point the full value of eddy viscosity is included. This method is particularly useful for flows experiencing pressure gradients since it is based on local conditions and has been recently popular for engineering studies of hypersonic vehicles. Yaghmaee and Roberts varied the onset threshold to match the transition point for the P8. Again, they did not specifically examine the affects of transition. The pitot pressure profile upstream of the cowl shock interaction compares well with the test data, indicating that the boundary layer approaching the interaction was simulated correctly.

7.0 COMMENTS

Based on the discussion of Section 2.0, it can be concluded that the state-of-the-art in modeling of the physics of high speed fluid flow is sufficient to yield an accurate simulation of typical inlet configurations, with a rather restrictive caveat on modeling of the turbulent boundary layer interactions. Commercial CFD codes are now available which include options for solving full Navier-Stokes, PNS, and Euler. These codes include perfect gas, equilibrium high temperature gas, and even finite rate chemistry models with broad ranges of chemical reactions from which to select.

The advanced numerical integration schemes mentioned in Section 3.0 are also sufficient to accurately simulate high speed inlet flows. Shock capturing capability with the advanced schemes is not a concern, although some experience is generally necessary in order to execute these advanced methods successfully. Commercial code developers often claim their products are "user friendly," but this always implies that new problems are easy to set up and initiate. It does not mean that users who are unfamiliar with aerodynamic theory and numerical methods can apply them successfully.

Grid generation tools have also been developed by government and industry which make this tedious task more automated but not independent of the skill and knowledge of the user. Current codes and grid generation tools are capable of multiblock grid solutions which are applicable to practically any supersonic inlet geometry. The complexity of an inlet application is limited by the size, cost, and availability of computer resources, not the software. New techniques for unstructured grids are making the grid generation task less demanding. These are currently being applied and validated, but no published results were available at the time of the literature survey.

Current techniques for boundary conditions discussed in Section 4.0 cannot be considered mature in all aspects. The typical specifications for small unit problems are clearly sufficient (freestream, extrapolation, solid walls). Issues such as wall pressure normal gradient and temperature conditions have either minor impact or their influence on the results are understood. However, great simplifications are necessary to implement numerical boundaries on realistic inlet configurations in order to limit the problem domain to a tractable size. Specifically, the bleed boundaries and diffuser exit boundaries are necessarily simplified, with questionable validity in some cases. New techniques for treating bleed boundaries appear promising. The author is aware of ongoing research in this area, both experimental and numerical. Techniques for improving diffuser exit boundaries are also under development which simulate the flow control characteristics of high speed engines.

Turbulence models are definitely the pacing technology issue for any CFD application which involves strong shock wave-boundary layer interactions. This issue does not need to be belabored, for there is exhaustive research in this area. In the mean time, continuous application and comparison with experiment is the standard operating procedure.

REFERENCES

1. MacCormack, R.W. and Baldwin, B.S., "A Numerical Method for Solving the Navier-Stokes Equations with Application to Shock- Boundary Layer Interactions," AIAA-75-0001, 13th Aerospace Sciences Meeting, Pasadena CA, January 1975.
2. Shang, J.S. and Hankey Jr., W.L., "Numerical Solution for Supersonic Turbulent Flow over a Compression Ramp," *AIAA Journal*, Volume 13, October 1975, pp. 1368-1374.
3. Anderson, D.A., Tannehill, J.C., and Pletcher, R.H., *Computational Fluid Mechanics and Heat Transfer*, Hemisphere Publishing Corp., U.S.A., 1984, pp. 221-235.
4. Anderson, J.D., *Modern Compressible Flow with Historical Perspective*, McGraw-Hill, 1990.
5. White, F.M., *Viscous Fluid Flow*, 2nd Ed., McGraw-Hill, 1991, pp. 539-561.
6. Agarwal, R., Deese, J., and Peters, G., "Transonic Shock/Boundary-Layer Interaction Studies--Asymptotic Theories, Numerical Solutions, and the Role of Turbulence," AIAA-88-3800, 1988.
7. Kunik, W.G., Benson, T.J., Ng, W., and Taylor, A., "Two- and Three-Dimensional Viscous Computations of a Hypersonic Inlet Flow," AIAA-87-0283, 25th Aerospace Sciences Meeting, Reno NV, January 1987.
8. Rhie, C.M., and Stowers, S.T., "Navier-Stokes Analysis for High Speed Flows Using a Pressure Correction Algorithm," AIAA-87- 1980, 23rd Joint Propulsion Conference, San Diego CA, June 1987.
9. Brenneis, A., and Wanie, K.M., "Navier-Stokes Results for Hypersonic Inlet Flows," AIAA-91-2472, 27th Joint Propulsion Conference, Sacramento CA, June 1991.
10. Gnos, A.V., Watson, E.C., Seebaugh, W.R., Sanator, R.J., and DeCarlo, J.P., "Investigation of Flow Fields within Large-Scale Hypersonic Inlet Models," NASA TN D-7150, April 1973.
11. Wilcox, D.C. and Traci, R.M., "A Complete Model of Turbulence," AIAA-76-351, 9th Fluid and Plasma Dynamics Conference, San Diego CA, July 1976.
12. Liou, M., Hankey, W.L., and Mace, J.L., "Numerical Simulation of a Supercritical Inlet Flow," AIAA-85-1214, 21st Joint Propulsion Conference, Monterey CA, July 1985.
13. Panaras, A.G., and Stanewsky, E., "Numerical Study of Secondary Separation in Glancing Shock/Turbulent Boundary Layer Interactions," AIAA-92-3666, 28th Joint Propulsion Conference, Nashville TN, July 1992.
14. Yaghmaee, S., and Roberts, D.W., "Modeling the Three- Dimensional Flow Through a Scramjet Inlet with a Hybrid PNS/PPNS Code," AIAA-88-2826, 24th Joint Propulsion Conference, Boston MA, July 1988.
15. *Air Intakes for High Speed Vehicles*, AGARD Advisory Report, AGARD-AR-270, September 1991, pp. 91-216.
16. Kim, Y.N., Buggeln, R.C., and McDonald, H., "Numerical Analysis of Some Supersonic Viscous Flows Related to Inlet and Nozzle Systems," AIAA-86-1597, 22nd Joint Propulsion Conference, Huntsville AL, June 1986.
17. Bissinger, N.C., and Eberle, A., "CFD Contributions During Hypersonic Airplane Intake Design," AGARD-CP-510, *CFD Techniques for Propulsion Applications*, February 1992.
18. Fujimoto, A., Niwa, N., and Sawada, K., "Numerical Investigation on Supersonic Inlet with Realistic Bleed and Bypass Systems," AIAA-91-0127, 29th Aerospace Sciences Meeting, Reno NV, January 1991.
19. Hindash, I., Bush, R., and Cosner, R., "Computational Modeling of Inlet Hammershock Wave Generation," AIAA-90-2005, 26th Joint Propulsion Conference, Orlando FL, July 1990.
20. Pordal, H.S., Khosla, P.K., and Rubin, S.G., "Transient Behavior of Supersonic Flow Through Inlets," AIAA-90-2130, 26th Joint Propulsion Conference, Orlando FL, July 1990.
21. Yang, H.Q., and Przekwas, A.J., "A Comparative Study of Advanced Shock-Capturing Schemes Applied to Burgers' Equation," *Journal of Computational Physics*, Volume 102, pp. 139-159.
22. Ong, C., and Knight, D., "Hybrid MacCormack and Implicit Beam- Warming Algorithms for a Supersonic Compression Corner," AIAA-86- 0204, 24th Aerospace Sciences Meeting, Reno NV, January 1986.
23. Visbal, M., and Knight, D., "The Baldwin-Lomax Turbulence Model for Two-Dimensional Shock-Wave/Boundary-Layer Interactions," AIAA-83-1697, 16th Fluid and Plasma Dynamics Conference, Danvers MA, July 1983.

24. Carroll, B.F., and Dutton, J.C., "Computation of Multiple Normal Shock Wave/Turbulent Boundary Layer Interactions," AIAA-902133, 26th Joint Propulsion Conference, Orlando FL, July 1990.
25. Benhachmi, D., and Greber, I., "Experimental and Numerical Investigation of an Oblique Shock Wave/Turbulent Boundary Layer Interaction with Continuous Suction," AIAA-89-0357, 27th Aerospace Sciences Meeting, Reno NV, January 1989.
26. Horstman, C.C., Hung, C.M., Settles, G.S., Vas, I.E., and Bogdonoff, S.M., "Reynolds Number Effects on Shock-Wave Turbulent Boundary-Layer Interactions - A Comparison on Numerical and Experimental Results," AIAA-77-42, 15th Aerospace Sciences Meeting, Los Angeles CA, January 1977.
27. Ramakrishnan, S., and Goldberg, U., "Numerical Simulation of Swept Shock/Boundary-Layer Interactions," AIAA-90-5234, 2nd International Aerospace Planes Conference, Orlando FL, October 1990.
28. Kapoor, K., Anderson, B.H., and Shaw, R.J., "Comparative Study of Turbulence Models in Predicting Hypersonic Inlet Flows," AIAA- 92-3098, 28th Joint Propulsion Conference, Nashville TN, July 1992.
29. Knight, D.D., "Numerical Simulation of Realistic High-Speed Inlets Using the Navier-Stokes Equations," *AIAA Journal*, Volume 15, November 1977, pp. 1583-1589.
30. Shang, J.S., Hankey Jr., W.L., and Law, C.H., "Numerical Simulation of Shock Wave - Turbulent Boundary-Layer Interaction," *AIAA Journal*, Volume 14, October 1976, pp. 1451-1457.
31. Shang, J.S., Hankey, W.L., and Petty, J.S., "Three-Dimensional Supersonic Interacting Turbulent Flow Along a Corner," *AIAA Journal*, Volume 17, July 1979, pp. 706-713.
32. Thompson, J.F., Warsi, Z.U.A., and Mastin, C.W., *Numerical Grid Generation - Foundations and Applications*, Elsevier Science Publishing Co., Inc., New York, New York, 1985.
33. *Numerical Methods for Engine-Airframe Integration*, edited by Murthy, S.N.B., and Paynter, G.C., AIAA Progress in Astronautics and Aeronautics, Volume 102, New York, New York, 1986.
34. Reddy, D.R., Benson, T.J., and Weir, L.J., "Comparison of 3-D Viscous Flow Computations of Mach 5 Inlet with Experimental Data," AIAA-90-0600, 28th Aerospace Sciences Meeting, Reno NV, January 1990.
35. Rizzetta, D.P., "Numerical Simulation of a Supersonic Inlet," AIAA-91-0128, 29th Aerospace Sciences Meeting, Reno NV, January 1991.
36. Knight, D., "A Vectorized Three-Dimensional Navier-Stokes Code for High Speed Inlets," Rutgers University, RU-TR-161-MAE-F, March 1984.
37. Knight, D.D., "Calculation of High-Speed Inlet Flows Using the Navier-Stokes Equations," *Journal of Aircraft*, Volume 18, September 1981, pp. 748-754.
38. Bush, R.H., "External compression Inlet Predicitons Using an Implicit, Upwind Multiple Zone Approach," AIAA-85-1521, 7th Computational Fluid Dynamics Conference, Cincinnati OH, July 1985.
39. Bush, R.H., "A Three Dimensional Zonal Navier-Stokes Code for Subsonic Through Hypersonic Propulsion Flowfields," AIAA-88-2830, 24th Joint Propulsion Conference, Boston MA, July 1988.
40. Knight, D.D., "A Hybrid Explicit-Implicit Numerical Algorithm for the Three-Dimensional Compressible Navier-Stokes Equations," AIAA-83-0223, 21st Aerospace Sciences Meeting, Reno NV, January 1983.
41. Hunter, L.G., Tripp, J.M., and Howlett, D.G., "A Mach 2.0 Plus Supersonic Inlet Study Using the Navier-Stokes Equations," AIAA-85- 1211, 21st Joint Propulsion Conference, Monterey CA, July 1985.
42. Shigematsu, J., Yamamoto, K., Shiraishi, K., and Tanaka, A., "A Numerical Investigation of Supersonic Inlet Using Implicit TVD Scheme," AIAA-90-2135, 26th Joint Propulsion Conference, Orlando FL, July 1990.
43. Hamed, A., and Lehnig, T., "An Investigation of Oblique Shock/Boundary Layer/Bleed Interaction," AIAA-90-1928, 26th Joint Propulsion Conference, Orlando FL, July 1990.
44. Hamed, A., and Lehnig, T., "The Effect of Bleed Configuration on Shock/Boundary Layer Interactions," AIAA-91-2014, 27th Joint Propulsion Conference, Sacramento CA, June 1991.
45. Hamed, A., Shih, S.H., and Yeuan, J.J., "An Investigation of Shock/Turbulent Boundary Layer/Bleed Interaction," AIAA-92-3085, 28th Joint Propulsion Conference, Nashville TN, July 1992.
46. Abrahamson, K.W., and Brower, D.L., "An Empirical Boundary Condition for Numerical Simulation of Porous Plate Bleed Flows," AIAA-88-0306, 26th Aerospace Sciences Meeting, Reno NV, January 1987.
47. Hsieh, T., Warlaw, A.B., and Coakley, T., "Numerical Simulation of a Ramjet Inlet Flowfield in Response to Large Amplitude Combustor Pressure Oscillation," AIAA-84-1163, 20th Joint Propulsion Conference, Cincinnati OH, June 1984.

48. Yoon, S., and Jameson, A., "An LU Implicit Scheme for High Speed Inlet Analysis," AIAA-86-1520, 22nd Joint Propulsion Conference, Huntsville AL, June 1986.
49. Gerbsch, R.A., and Agarwal, R.K., "Computation of Hypersonic Ramjet Inlet Flowfields Using an Upwind Parabolized Navier-Stokes Code," AIAA-88-2828, 24th Joint Propulsion Conference, Boston MA, July 1988.
50. Campbell, A.F., and Syberg, J., "Design Study of an External Compression Supersonic Inlet Using a Finite Difference Two-Dimensional Navier-Stokes Code," AIAA-84-1275, 20th Joint Propulsion Conference, Cincinnati OH, June 1984.
51. Sakowski, B., Darling, D., Roach, R.L., and van de Wall, "Evaluation and Application of the Baldwin-Lomax Turbulence Model in Two-Dimensional, Unsteady, Compressive Boundary Layers with and without Separation in Engine Inlets," AIAA-92-3676, 28th Joint Propulsion Conference, Nashville TN, July 1992.
52. Bloesch, E., Carroll, B.F., and Morris, M.J., "Numerical Simulation of a Confined Transonic Normal Shock Wave/Turbulent Boundary Layer Interaction," AIAA-92-3668, 28th Joint Propulsion Conference, Nashville TN, July 1992.
53. Knight, D.D., "Calculation of a Simulated 3-D High Speed Inlet Using the Navier-Stokes Equations," AIAA-83-1165, 19th Joint Propulsion Conference, Seattle WA, June 1983.
54. Ng, W.F., Ajmani, K., and Taylor, A.C., "Turbulence Modeling in Hypersonic Inlets," AIAA-88-2957, 24th Joint Propulsion Conference, Boston MA, July 1988.
55. Wilcox, D.C., "Reassessment of the Scale-Determining Equation for Advanced Turbulence Models," AIAA-84-0176, 22nd Aerospace Sciences Meeting, Reno NV, January 1984.
56. Lowrie, B.W., "A Multi-Zone $k-\epsilon$ Turbulence Model for Complex Configurations," AIAA-90-2001, 26th Joint Propulsion Conference, Orlando FL, July 1990.
57. Povinelli, L.A., "Computational Modeling and Validation for Hypersonic Inlets," NASA TM 103111, 75th Symposium on Hypersonic Combined Cycle Propulsion, Madrid, Spain, May-June 1990.
58. Weir, L., Reddy, D.R., and Rupp, G., "Mach 5 Inlet CFD and Experimental Results," AIAA-89-2355, 25th Joint Propulsion Conference, Monterey CA, July 1989.
59. Tennekes, H., and Lumley, J.L., *A First Course in Turbulence*, MIT Press, Cambridge, Massachusetts, 1990.
60. Knight, D.D., "Improved Calculation of High Speed Inlet Flows: Part I. Numerical Algorithm," *AIAA Journal*, Volume 19, January 1981, pp. 34-41.
61. Knight, D.D., "Improved Calculation of High Speed Inlet Flows: Part II. Results," *AIAA Journal*, Volume 19, February 1981, pp. 172-179.
62. Mace, J., and Hankey, W., "Review of Inlet-Airframe Integration Using Navier-Stokes Computational Fluid Dynamics," AIAA-84-0119, 22nd Aerospace Sciences Meeting, Reno NV, January 1984.
63. Talcott, N.A., and Kumar, A., "Numerical Simulation of Flow Through Inlet/Diffusers with Terminal Shocks," AIAA-84-1362, 20th Joint Propulsion Conference, Cincinnati OH, June 1984.
64. Kerlick, D.G., "Adaptive Mesh Solution for Supersonic Conical Flow in a Rectilinear Inlet," AIAA-85-1626, 18th Fluid Dynamics and Plasmadynamics and Lasers Conference, Cincinnati OH, July 1985.
65. Shang, J.S., "An Assessment of Numerical Solutions of the Compressible Navier-Stokes Equations," *Journal of Aircraft*, Volume 22, May 1985, pp. 353-370.
66. White, M.E., Drummond, J.P., and Kumar, A., "Evolution and Status of CFD Techniques for Scramjet Applications," AIAA-86-0160, 24th Aerospace Sciences Meeting, Reno NV, January 1986.
67. White, J.A., and Rhie, C.M., "A Full Navier-Stokes Analysis of a Three Dimensional Hypersonic Mixed Compression Inlet," AIAA-88-3077, 24th Joint Propulsion Conference, Boston MA, July 1988.
68. Reddy, D.R., Smith, G.E., Liou, M.F., and Benson, T.J., "Three-Dimensional Viscous Analysis of a Hypersonic Inlet," AIAA-89-0004, 27th Aerospace Sciences Meeting, Reno NV, January 1989.
69. Cooper, G., and Sirbaugh, J., "The PARC Distinction: A Practical Flow Simulator," AIAA-90-2002, 26th Joint Propulsion Conference, Orlando FL, July 1990.